On the Mechanical Properties and Failure of Low-Pressure Cold-Sprayed Tungsten Carbide-Nickel Metal Matrix Composite Coatings

by

Guriqbal Singh Munday

A thesis submitted in partial fulfillment of the requirements for the degree of

Master of Science

Department of Mechanical Engineering

University of Alberta

Abstract

Tungsten carbide-Nickel (WC-Ni) metal matrix coatings (MMC) were fabricated using a low-pressure cold spray unit. The coatings were designed according to 50, 71, and 92 weight percentages of WC in the feedstock powder. These coatings were subsequently prepared for uni-axial quasi-static tensile testing to evaluate their mechanical properties, namely the tensile strength, the Young's modulus, and the toughness. Further, the evolving strains during tensile testing were computed using the Digital Image Correlation (DIC) technique. The coatings were characterized for their microstructure, namely the total particle-matrix interfacial area, the mean free path between the particles, the average particle size, and the porosity of the coating by image analysis on the captured scanning electron microscope (SEM) micrographs. The results indicate that with an increase in the content of WC in the coatings, there was an increase in tensile strength, strain to failure, Young's modulus, and the toughness of the coatings. This increase was attributed to the refined microstructural features that occurred with the decrease in the porosity of the coating that was caused by the greater consolidation of the Ni matrix at higher WC content in the metal matrix. Additionally, this improvement was linked to the increase in the particle-matrix interfacial area caused by the increase in carbide content, a decrease in the average WC particle size in the coating, and a reduction in the mean free path between the WC particles. Using this quantification of key microstructural features and mechanical properties, a combined microstructural feature's effect on the tensile strength based on the individual functional relationships between the microstructure and mechanical properties was also explored. This revealed that there exist distinct tensile strength regimes based on the content of WC wt.% in the coatings. The coatings with content of WC beyond 30 wt.% reported a significant increase in

their tensile strength. This was reiterated to the refined microstructure at higher content of WC in the coating and their ability to absorb higher mechanical energy to failure. Next, damage in the coatings was quantified by calculating the Poisson's ratio and it was used to explain the tensile failure of the coatings. The coatings with WC content less than 15 wt.% were accompanied with higher damage than the coatings with WC content beyond 30 wt.%. Finally, a preliminary exercise is presented to model the tensile stress-strain behaviour of the tested coatings with the application of the cohesive zone between the metal matrix and the reinforcing phase. The modelling results indicated that the failure strength of the cohesive zone was approximately 215 MPa for 15 wt.% WC in the coating. The model also suggests that the tensile strength of the coating increases with an increase in particle-matrix interface strength. The mechanical properties and the microstructural data collected in this thesis is imperative to validate mechanism-based models to predict the stress-strain response and the performance of cold sprayed MMCs. Overall, besides quantifying the mechanical properties of the low-pressure cold-sprayed WC-Ni MMC coatings, this thesis study emphasizes the importance of tailoring the microstructure of cold spray MMC coatings to develop the next generation of coatings with improved mechanical properties and performance.

Acknowledgements

I echo the thanks to my supervisors, Dr. André McDonald and Dr. James Hogan. Their constant guidance is behind the successful completion of this thesis. They render continuous support with their expertise in mechanical and materials engineering. I am also indebted to Dr. McDonald for providing me with an opportunity to be a part of his research group and to attend various professional activities during the program. I am also indebted to Dr. Hogan for his thoughtful discussions and his mentorship in analyzing and delivering of the data.

Further, I pay my sincere gratitude to all the supporting staff at the University of Alberta. I would like to thank all the colleagues and friends for their fruitful discussions. Special thanks to the people at the Center for Design of Advanced Materials at the University of Alberta for their help with the tensile experiments. I also express my gratitude to the MITACS programme for providing partial funding for the program and providing me with an opportunity, which enhances my knowledge in the field of research.

In the end, I thank my family and friends, who provided continued support even during the difficult times throughout the research period. This thesis would not have been possible without their continuous encouragement to pursue master's studies at the University of Alberta, Canada.

Contents

List of Figures

List of Tables

Glossary of Symbols

a effective material coefficient

C stiffness matrix $\left(\frac{\mathrm{N}}{\mathrm{m}}\right)$

E stress-free strain

f volume fraction of particles

H hardness $\left(\frac{\mathrm{kg}}{\mathrm{mm}^2}\right)$

$\mathbf{B}$ strain concentration tensor

I ellipsoidal volume (m^3)

l arbitrary function

S surface area of inclusion

$\mathbf{u}$ displacement vector (m)

V volume of the arbitrary body

W wear $\left(\frac{\mathrm{mm}^3}{\mathrm{Nm}}\right)$

x global coordinate

y local coordinate

Greek symbols

v volume fraction

ζ Eshelby tensor

Ω heterogeneous solid body

φ yield function

σ stress $\left(\frac{\mathrm{N}}{\mathrm{m}^2}\right)$

$\overline{\sigma}$ mean stress $\left(\frac{\mathrm{N}}{\mathrm{m}^2}\right)$

$\overline{e}$ mean strain

$\varepsilon(x)$ constrained strain

κ ratio of length scales

$\bar{\varepsilon}$ accumulated strain

ϕ average reinforcing particle size

θ porosity

λ mean free path

Ψ particle-matrix interfacial area

Subscripts

upper upper bound

lower lower bound

r reinforcement

i matrix index

j matrix index

k matrix index

m matrix

M mean

l matrix index

0 infinite body

1 ellipsoidal inclusion

y yield

Superscripts

ε cell dimension dependent variables

p plastic

1 Introduction

1.1 Wear

The continuous interaction of mechanical equipment with hard-faced particles causes wear and corrosion of equipment in the Oil & Gas and Mining industries [1]. Consequently, this wear and corrosion causes the structural degradation of the mechanical equipment and results in their premature failure [2, 3]. Thus, a significant portion of revenue of the industry is directed towards the maintenance and protection of the mechanical equipment [3, 4]. In the oil and gas industry, the wear mainly comprises of the impact wear, the erosive wear, and the abrasive wear [4]. Impact wear is caused by the continuous impact of big pieces of rocks, which is prevalent in accessories and machinery such as screens or crushers used in the processing of oil sands [4]. Erosive wear is caused by the fluid, which contain hard solid particles and flows over the mechanical equipment. Generally, erosive wear occurs due to the transportation of oil sand slurries. The slurries containing hard alumna particles, which typically interact with the equipment surface, causing erosive wear [2, 4, 27] (see Fig. 1). Abrasive wear occurs in the transportation of the sand [4]. The sand slides over and between the surfaces, causing equipment's surface material loss over time. Therefore, to avoid the detrimental effects of wear to the mechanical equipment, protection by surface modification of equipment is desired [5–7]. The surface modification by the depositing the hard-faced sacrificial coatings is ubiquitous in the mining industries [7, 8].

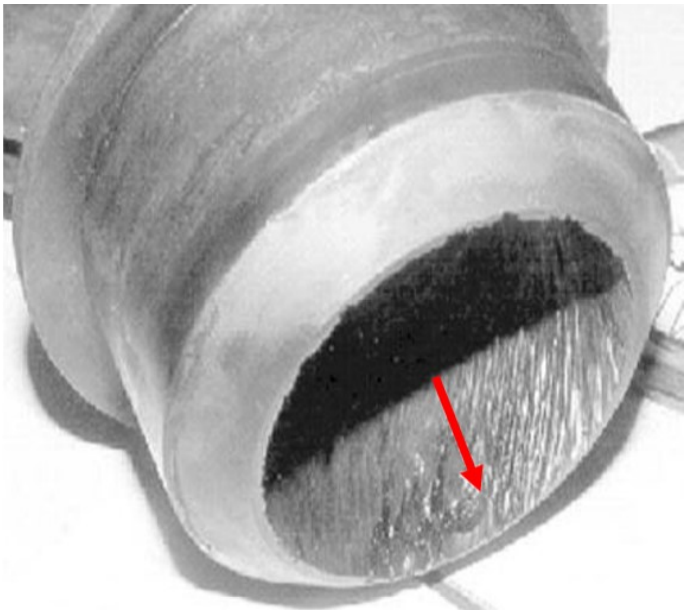

Figure 1: Erosive wear of the mechanical equipment. The arrow marks the material removed from the equipment [27].

1.2 Metal matrix composite coatings

Multi-phase composites or metal matrix composites (MMC) are composite materials that are comprised of at least two constituent phases, where one of those phases is metallic, and the other reinforcing phases may be different metals or other materials such as a ceramics, inorganic materials, or organic materials. These types of composite materials are desirable because they offer enhanced properties resulting from the combination and synergies of the properties of both the matrix and the reinforcing materials, such as light weight, strength, stiffness, wear resistance, creep resistance, and improved electrical and thermal conductivity [6]. The distinct characteristics of MMCs such as wear resistance, corrosion resistance, and thermal resistance

have made them ubiquitous in the Oil and Gas industry, Aerospace industry, Defense industry, and for use in cutting tools [5–13].

1.3 Fabrication of metal matrix composites

Metal matrix composites may be fabricated by using commercially available methods such as the liquid state method [5], the solid-state method [5], and thermal spraying [4, 14, 15], to name a few. In the liquid state method, the reinforcing particles are introduced into the stream of molten metal. The flow of molten metal facilitates the manufacture of near net shape structures; however, the process limits the control of the distribution of the reinforcing phase in the matrix. Also, during melt infiltration, the particles may agglomerate and settle in the matrix [5]. The solid-state method consists of pressing a solidifying powder that contains the particulates to approximately 75% of the initial density of the powder. After pressing, the consolidated material may be extruded, rolled, or forged to the desired shape. In general, the solid-state method provides for higher overall strength in the MMC than that fabricated by way of the liquid state method [5].

Thermal spraying, which includes plasma spraying, high-velocity oxy-fuel (HVOF) spraying, wire-arc spraying, flame spraying, and cold spraying [14, 15], is a highly scalable manufacturing process that is currently used to fabricate MMC-based thin coating systems from mechanically blended or fused powders. Cold spraying is a coating deposition method in which powder particles are accelerated to supersonic velocity through a de Laval nozzle (see Fig. 2). The powder particles adhere to the substrate, accumulate, and produce a coating on the surface [12–

20]. The fact that the deposition temperature in cold spraying is lower (0-700°C [14]) than that in the other thermal spray processes (for example, 8000-10,000°C in plasma spraying [14], 11,000-14,000°C in wire-arc spraying [14], and 2000-3000°C in flame spraying [14],) results in fabricated coatings that are nearly devoid of oxidation, decarburization, metallurgical transformations, and thermal stresses [13, 14, 21–23]. Further, the incorporation of the hard particles in the feedstock powder to fabricate the MMC coatings has been determined by multiple factors. The reinforcement particles in the feedstock powder improves the deposition efficiency of the blended powders due to the impact of hard incoming particles on the previously deposited layers. As shown in Fig. 3, an increase in the weight percent (wt.%) of tungsten carbide (WC) in the feedstock powder from 50 to 96 wt.%, resulted in an increase in the wt.% of WC in the coating from approximately 7 ± 0.9 to 68 ± 0.5 wt.% [25]. In addition, a decrease in porosity was observed due to greater consolidation of the metal matrix at higher content of hard reinforcing particles [12, 24–26]. The volumetric percent (vol.%) of the porosity in the coating decreased from approximately 2 ± 0.7 to 0.3 ± 0.1 vol.% with a change in the powder blend from 50 wt.% WC + 50 wt.% Ni to 96 wt.% WC + 4 wt.% Ni [10]. Further, Lee, *et al.* [15, 28], and Xie, *et al.* [27] have reported that composite coatings consisting of a hard-reinforcing phase may significantly improve the wear resistance in pumps used for oil sands operations. Thus, cold spraying provides one promising alternative method for fabrication of MMC coatings.

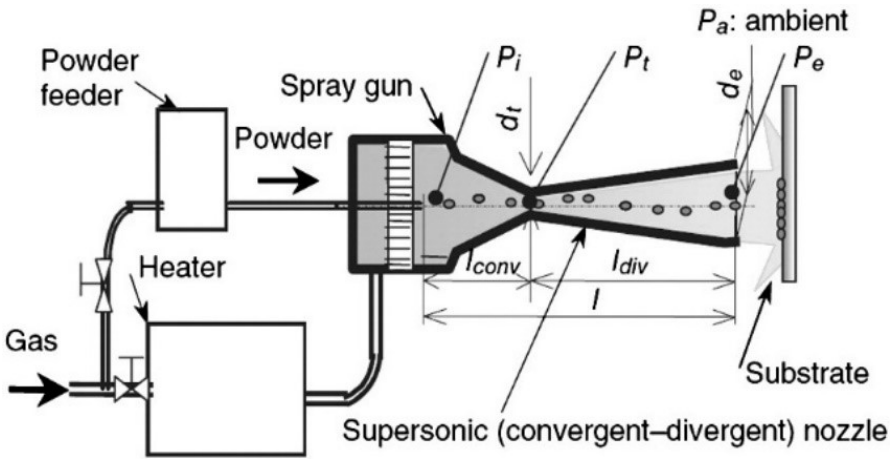

Figure 2: Schematic of the cold spray process [17].

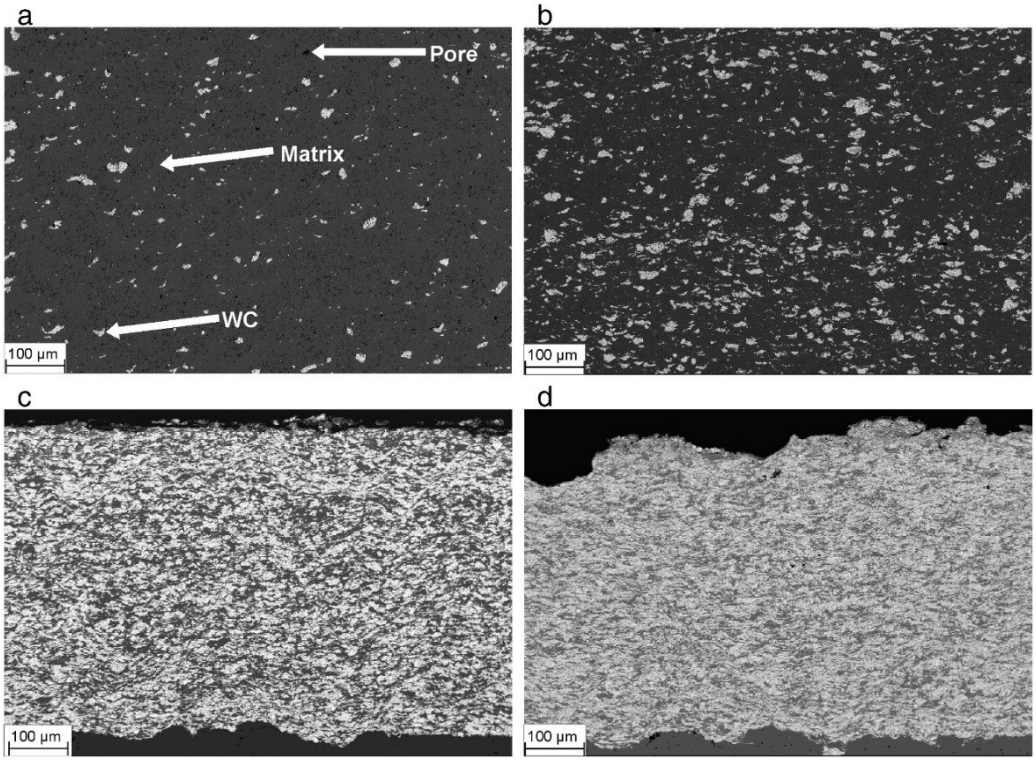

Figure 3: SEM image of the microstructure of cold-sprayed MMC coatings fabricated from feedstock with composition of (a) 50 wt.% WC + 50 wt.% Ni; (b) 75 wt.% WC + 25 wt.% Ni; (c) 92 wt.% WC + 8 wt.% Ni; and (d) 96 wt.% WC + 4 wt.% Ni [25].

1.4 Motivation

WC-based MMC coatings are ubiquitous in Oil and Gas industry due of their remarkable wear resistance [14, 26, 28]. Most of the fundamental understanding to characterize the performance of these coatings is based on localized testing systems such as hardness testing [14, 25, 26]. However, researchers have noted that the results obtained from hardness testing may not be the correlated in predicting the macro- mechanical response of coatings [32, 33, 36, 62]. They have noted that the macro response of the coatings is greatly influenced by the microstructure of the coating [32, 33, 36]. Many studies are available in the literature where the performance of wear resistant coatings is predicted based on the Hardness of those coatings [15, 25, 26]. However, limited studies are available where researchers have tried to conduct a full field testing of cold sprayed coatings such as tensile testing. Recently researchers have reported tensile strength data for the coatings fabricated using the thermal spray process [62], however, limited researchers have explored the mechanical properties such as the Young's modulus, tensile strength, toughness, and Poisson's ration of low-pressure cold sprayed MMCs. Therefore, this study develops a methodology to extract the firsthand data on these mechanical properties for the low-pressure cold sprayed WC-Ni MMC coatings. Also, the macro behaviour of the coatings is highly influenced by the microstructure of the MMC, namely particle size, mean free path, interfacial area between the reinforcing particle and metal matrix [9, 15, 24]; however, limited studies are available for the cold sprayed carbide based MMCs. Therefore, to better understand the influence of microstructure on the macro response of the cold sprayed WC-based coatings, a comprehensive study must be conducted.

1.5 Objectives

Broadly, the objective of this thesis was to evaluate and understand the microstructure-dependent material properties and failure behaviors of the cold sprayed WC-Ni MMC coatings. The current study explores the tensile stress-strain responses of the fabricated coatings under quasi-static loading rates with specific goals to:

1. Fabricate a high strength coating by varying the content of WC wt.% in the coating.
2. Determine the mechanical properties of the composite by conducting uniaxial tensile tests.
3. Explore and analyze the use of the digital image correlation technique in the field testing of cold sprayed coatings.
4. Study the effect of reinforcing particle content on tensile strength of the fabricated coatings.
5. Study the effect of mean free path between the reinforcing particles on tensile strength of the fabricated coatings.
6. Study the effect of average particle size on tensile strength of the fabricated coatings.
7. Study the effect of porosity on tensile strength of the fabricated coatings.
8. Investigate the combined effect of carbide content, particle-particle mean free path, average particle size, and porosity on tensile strength of the fabricated coatings.
9. Determine and investigate the link between the mechanical energy absorbed to failure by the coatings and the corresponding tensile strength.

10. Quantification of damage and study its influence on the tensile strength of the coatings.
11. Numerically model and validate the tensile stress-strain behaviour of the cold sprayed WC-Ni MMC coatings.

1.6 Thesis organization

This thesis manuscript is organized into several chapters. Chapter 2 describes the literature review for extracting and estimating the wear performance and mechanical properties of the MMCs. This chapter also provides a comprehensive review of the empirical and the numerical models employed to predict the mechanical properties and wear performance of the MMCs. Chapter 3 describes the experimental procedure used to fabricate and characterize the cold sprayed WC-Ni MMC coatings. Chapter 4 presents the results and discuss the objectives of this study. Further, Chapter 5 documents the conclusions from this research and finally Chapter 6 outlines the future work and recommendations. Appendix A documents the MATLAB code used to plot the tensile stress-strain curves and Appendix B provide additional SEM images of the microstructure of the three different blended powders.

2 Background on Performance Testing and Modelling

2.1 Testing of MMC coatings for wear applications

The improvement in the wear performance of mechanical equipment due to surface modification is primarily characterized via experiments, which predominantly describe the wear resistance/wear rate of the MMC coating under controlled testing. Standard test methods such as ASTM G65 for abrasion resistance, as shown schematically in Fig. 4 (a) [29], and ASTM G99 for the pin on disc test, also shown in Fig. 4b [30], are the most prominent standard wear tests for coating materials. Most researchers [15, 28, 31–39] conduct these tests to characterize the wear performance of MMC coatings and quantify the wear rates of the coatings undergoing abrasion and erosion testing.

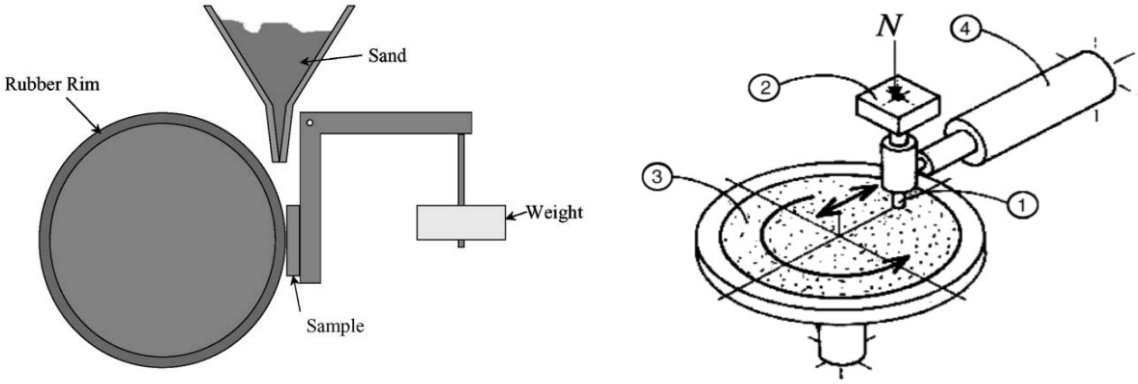

(*a*) (*b*)

Figure 4: Test assemblies for (*a*) the ASTM Standard G65 [29] and (*b*) the ASTM Standard G99 tests [30].

The standard test methods are useful for comparing the performance of a particular MMC coating based on a chosen benchmarked performance parameter, which is generally material loss during the tests [41]. The tests produce data that can be used to establish relationships between mechanical properties such as hardness and toughness and the measured material loss on a macro length scale. Visual assessment and characterization of the wear scars of the tested samples may be useful to predict the failure mode of the MMC coating from three foundational failure mechanisms of MMC coatings, namely: 1. brittle fracture of the particle reinforcement due to its lower toughness; 2. failure of the metal matrix due to the ductile failure of the binder metal; and 3. failure at the interface between the reinforcing particle and the metal matrix [31, 34, 42–45]. Moreover, the results from the standard tests are used as input parameters into numerical models of the performance of the coatings and to validate other models [33].

2.2 Introduction to modelling of mechanical properties

The experimental characterization of MMC coatings is essential; however, there are major drawbacks. These standard tests are limited by the test assemblies and the abrasive media, if any, that are used to induce wear in the coating materials; this may not be truly indicative of the multi-faceted wear mechanisms that occur in practice [36]. Moreover, the laboratory experiments are arduous and expensive to perform. These limitations and constraints on experimental testing of the MMC coatings warrant the need for modeling of the mechanical properties and behavior of the MMC coatings in order to understand the wear performance of coatings better under various applied loading conditions [32, 33, 35].

Several factors have motivated the desire to pursue modelling studies of particle-reinforced metal matrix composite coatings. As noted by Holmberg, *et al.* [32, 33], modelling of MMC coatings reduce the time required to develop a tailored microstructure, provide more in-depth insight into the mechanical properties, and allows to study the complex wear removal processes of the coatings. Also, according to Qing [34], virtual tests enable researchers to load a composite material multi-axially, as well as study the detailed microscale stress-strain fields and failure evolution in the coating, which may inform on the development of architectured microstructures. Today, numerous successful applications of MMC coatings for wear resistance in the Aerospace industry [9, 31], Defense industry [9, 13], Oil and Gas industry [3, 15], and in Cutting Tools [27, 41] are described in the literature. Therefore, a brief overview of the model development of the mechanical behavior of MMC coatings to is presented in this section of the thesis.

2.2.1 Empirical models

The empirical models have been developed in an effort to provide estimates of and predict the mechanical properties (e.g., hardness [15], and elastic modulus [44]) of MMC coatings. The seminal modelling of the mechanical properties of MMC coatings was undertaken by Garrison [37] and Axen and Jacobson [39], where they proposed "bounds" on the effective hardness of the MMC, assuming either iso-strain condition per the Voigt model of Eq. 1a, or iso-stress condition per the Reuss model of Eq. 1b. Equations 1a and 1b are given as,

$$H_{\text{upper}} = v_{\text{r}} H_{\text{r}} + v_{\text{m}} H_{\text{m}}, \tag{1a}$$

$$H_{\text{lower}} = \left(\frac{v_{\text{r}}}{H_{\text{r}}} + \frac{v_{\text{m}}}{H_{\text{m}}} \right)^{-1}, \tag{1b}$$

where, H ($\mathrm{kg\,mm^{-2}}$) represent the hardness value and the subscripts upper and lower in H represent the upper bound and the lower bound of hardness, respectively. H_{r} and H_{m} are the hardness values of reinforced and matrix phases, and v_{r} and v_{m} are the volume fractions of reinforced and matrix phases, respectively.

Based on the similar approach of a linear combination of material properties, the classical bounds for the quantification of wear were proposed. The proposed linear rule of mixtures (Equation 2a, Upper bound) and the inverse rule of mixtures (Equation 2b, Lower bound) were based on the continuum mechanics approach, neglecting the field fluctuations at the microstructural level [42]. Further, these equations were overly simplified regarding the constituent's contribution towards wear resistance and are valid only if the abrasive wear rate of constituents is proportional to the applied load [39]. These relations are equivalent for the estimation of both mechanical properties and wear.

$$W_{\mathrm{upper}} = v_{\mathrm{r}} W_{\mathrm{r}} + v_{\mathrm{m}} W_{\mathrm{m}}, \tag{2a}$$

$$W_{\mathrm{lower}} = \left(\frac{v_{\mathrm{r}}}{W_{\mathrm{r}}} + \frac{v_{\mathrm{m}}}{W_{\mathrm{m}}} \right)^{-1}, \tag{2b}$$

where, W $\left(\mathrm{mm^3 N^{-1} m^{-1}}\right)$ represent the wear rate and the subscripts upper and lower in W represent the upper bound and the lower bound of wear rate, respectively. W_{r} and W_{m} are the

wear rate values of reinforced and matrix phases, and v_r and v_m are the volume fractions of reinforced and matrix phases, respectively.

In 1994, Axen, *et al.* [39] reformulated the Archard's equation to explain the experimental Pin-on-disc test results for the MMCs. The equation is based on assuming the wear rate of metal to be proportional to both applied load and sliding distance of the pin. This assumption is further extended for composites by considering the equal wear (EW) and the equal pressure (EP) theories. A state of EW in a composite is a preferred wear state as both phases of the MMC worn in parallel providing the maximum possible resistance. So, this provides the upper bound estimation of wear resistance or the lower bound estimate of wear rate. Similarly, a state of EP, which assumes of uniformly distributed load over the composite, provides the lower bound for wear resistance. In this, the reinforcement contributes minimum towards wear resistance as it shares a lower load due to its less effective area in the composite. Figure 5 shows that for an EW state, the specific resistance of the silicon carbide reinforced aluminum MMC in a pin on disc test is higher than the corresponding wear resistance in an EP wear condition. Corollary, wear rate for the silicon reinforced aluminum MMC is higher in an EP condition than the wear rate in EW condition. The detailed mathematical derivation on these theories may be found in the paper by Axen, *et al.* [39].

The empirical models are frequently used and in a recent study to characterize the wear performance of low-pressure cold spraying manufactured coatings, Lee, *et al.* [28] showed that Hardness is one of the main factors in determining the performance of the composite coatings in wear tests. This was also observed by Melendez, *et al.* [25, 26], Gant, *et al.* [35], and Axen, *et al.* [39] while studying wear rates of composite coatings. Lee, *et al.* [28] showed that by increasing

the hardness of the coating, the wear rate decreases (see Fig. 6). Figure 6 shows the Hardness versus wear rate plot for three different MMC coatings fabricated by low-pressure cold spraying unit.

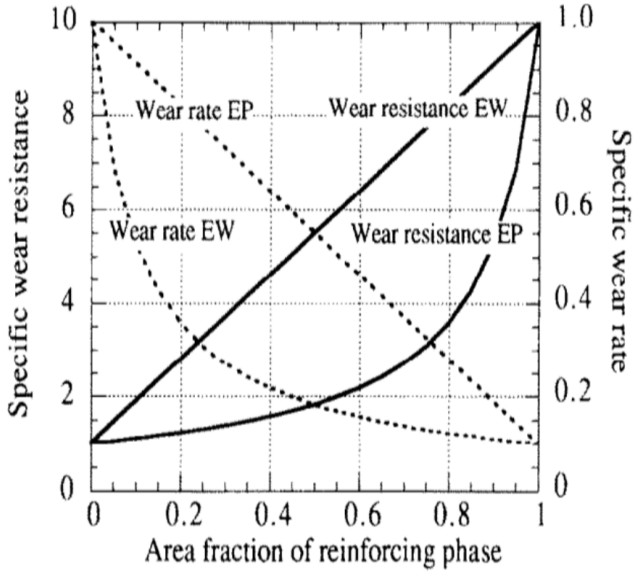

Figure 5: The equal wear and equal pressure rules of mixture plotted in terms of both wear resistance and wear rate [39].

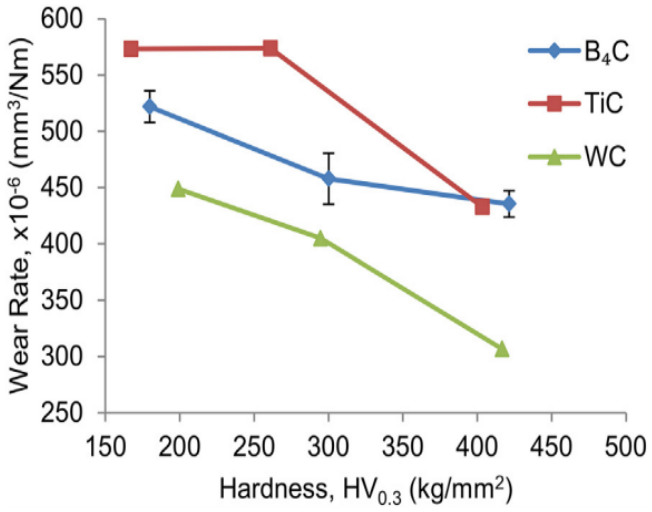

Figure 6: Hardness versus wear rate plot for a standard ASTM G65 test with three different MMC coatings fabricated by low-pressure cold spraying unit [28].

Thus, based on the reported experimental work on MMC coatings, it may be assumed that the hardness of the coating determines the wear performance of the coatings. However, the results from Holmberg, *et al.* [33] for a wear test found mild correlation with the hardness of the particle and the matrix. Thus, characterization of wear based on a single mechanical property like Hardness could be misleading or overstated. In addition, researchers [42-44] noted that the composites behave differently than from continuum analysis due to the non-linear mechanical properties mismatching at the interface. Also, Torrance [36] points out that the wear resistance of a composite is a function of the shape of the abrasive particles with angular particles causing more wear than the rounded abrasive particles. Today, there is a common consensus among researchers [9, 31, 32, 42-47] that, in fact, the macro response of the multiphase materials is governed by the microstructural features such as shape, size, mean free path, and orientation of particles and the models need to incorporate these to predict the mechanical response accurately (see Fig. 7). As an example, Figure 7 shows that the model (left side in figure) deprived of the microstructural features, results in the averaged stress field response on the macro scale under the indentation load. Further, the model (right side in figure) which incorporates the microstructure of the material shows the stress concentration at the interface of the matrix and the reinforcement. This stress mismatch at the interface may result in interface debonding which is one of the main failure mechanisms as discussed previously.

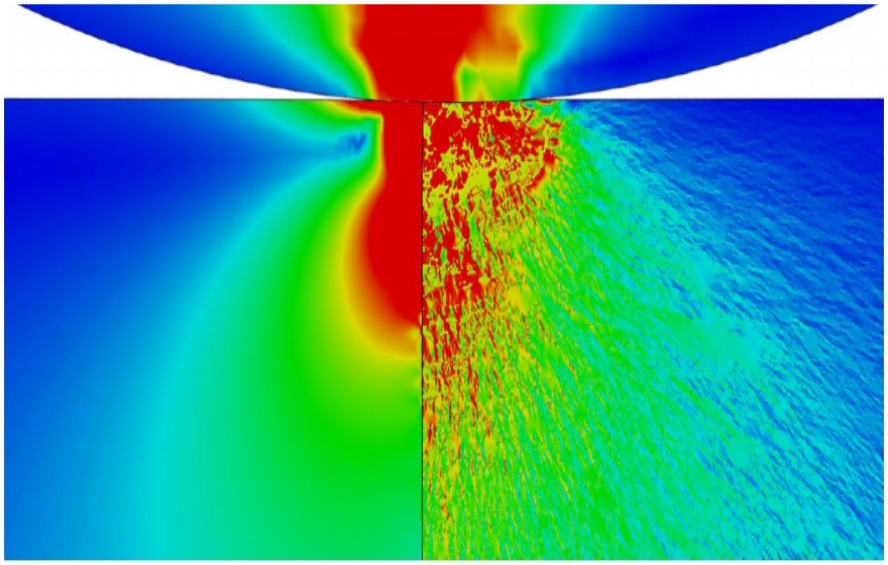

Figure 7: Difference between the stress field, (left) from a model devoid of microstructural properties; (right) to a model accounting for microstructural properties for an indentation test [17].

As discussed, there are numerous criteria established for specifying the bounds (for example, Voigt model and Reuss model [37, 39]) that are available in the literature to estimate the mechanical properties like hardness and elastic modulus of the MMC. Even though the theoretical simplicity of these models is attractive, but they are not the correct representation of the actual mechanical behaviour of MMC composite. So, to incorporate the microstructural features, according to Chawla, *et al.* [9], this leads us to have simulations rather than empirical models.

2.2.2 Numerical simulations

To understand better the influence of microstructural features on the macro-response of MMC coatings, there is a growing trend among researchers to model the MMC coatings numerically [9, 32, 33, 42–51]. This understanding of micro-macro relationship may lead the researchers to determine the critical variables that affect the mechanical response of the MMC coatings. Though there is no explicitly available numerical model for cold sprayed fabricated MMC coatings, there are a few related works on modelling the behavior of ceramic-metal materials in other disciplines (e.g., thermal spraying [32], laser cladded MMC coatings [33], to name a few). In this section of the thesis, we review some previous work on microstructure and physics-based modelling on ceramic-metal materials and make links to sprayed MMC coatings where applicable.

For numerical simulations, the heterogeneity of the MMC in the geometry may be incorporated in the models through generation of randomly distributed particles, which is mainly achieved via two methods [47]. The first method is the tessellation of 2-D or 3-D images of MMC microstructure [47] and second, via Representative Volume Element (RVE) - a statistical equivalent of the microstructure (see Fig. 8) [9]. Figure 8 shows the different shapes of the reinforcing particles that may be incorporated in the metal matrix (suppressed in figure). Here, the volume fraction of the reinforcing particles may be calculated using the image analysis of the microstructure, for example, election microscopy imaging [47]. Though more realistic, the intended application range of the first method is limited due to the computational time efficiency because the whole meshed body is solved numerically instead of its statistical equivalent [47]. In

contrast, the second method of generating RVEs or unit cell model gained popularity due to its computational time efficiency as a result of a smaller number of meshed parts to be solved numerically and is employed to understand the response of the composite undergoing mechanical loading [42, 47]. Further, the selection of the length scale of the RVE is of paramount importance. It should be small enough to be computationally efficient and large enough to accurately represent the microstructure [42, 43]. As noted by Holmberg, *et al.* [32, 33], these ideal microstructures without considering defects and voids may provide the first insight into the critical/dominating parameters on the mechanical response.

In order to compute the macro-structural behaviour of the multi-phase composites, the RVE is assigned to each macro point of the structure and is discretized using the finite elements. The microscopic stresses and strains in the RVE may be computed from a known constitutive equation and subsequently, macro stresses and strains are defined as the volume averages at the equilibrium. The following section provides an overview of the most relevant constitutive equations work from the literature to describe the mechanical response of ceramic-metal materials.

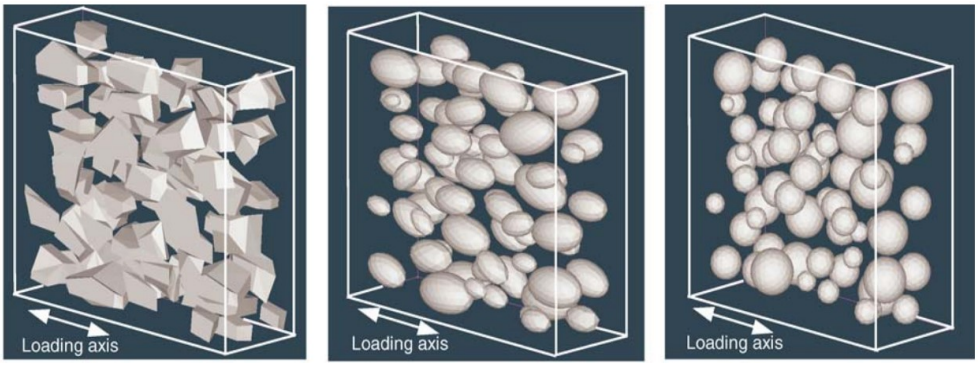

Figure 8: Representation of the RVE's with different shapes of the reinforcing phase: (from left to right) angular; ellipsoidal; and spherical [9].

2.2.2.1 Asymptotic homogenization

Stresses and strains at the micro and macro level may be computed using the asymptotic homogenization. This technique is derived in [43] and is mainly employed for the periodic structure but may also be extended to nonlinear case. Figure 9 shows the periodic structure with distinguished macroscopic and microscopic length scales. In the figure, the macroscopic length scale is in the order of magnitude of dimension of heterogeneous body and microscopic length scale scales the constituents of the heterogenous body. The macroscopic or the global coordinate vector, *x*, is related to microscopic or the local coordinate vector, *y*, according to Eq. 3, where κ is the ratio of the scales.

$$y = \frac{x}{\kappa} \tag{3}$$

It follows from Eq. 3 that, as κ tends to zero, the solution using the asymptotic technique for the periodic body is also applicable to the heterogeneous body. This is because when a macroscopic point in a heterogeneous body is zoomed in to reach the level of its constituents, the homogenization problem effectively reduces to same solution as of single particle homogenization.

To formulate the constitutive equation using the asymptotic technique, consider a heterogeneous body, Ω, defined by the balancing Eq. 4, constitutive Eq. 5, strain by Eq. 6, and boundary condition by Eq. 7 [43],

$$\sigma_{ij}^{\varepsilon}(x) + l_i(x) = 0, \tag{4}$$

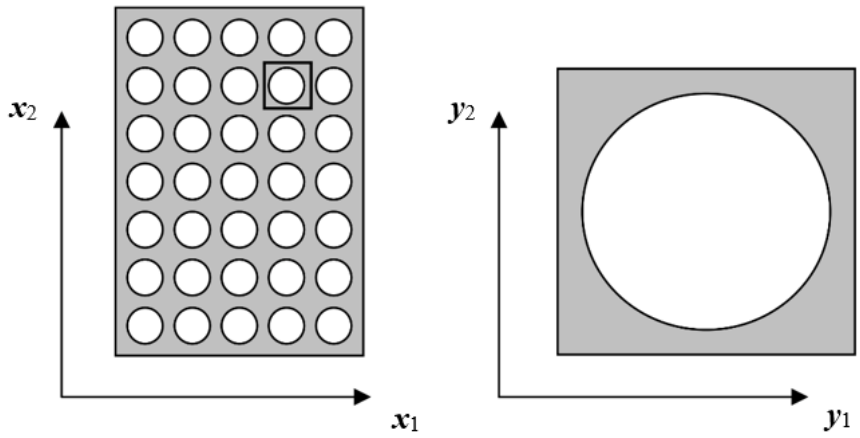

Figure 9: Two distinguished length scales: (left) Macroscopic scale, *x*; and (right) microscopic scale, *y* [43].

$$\sigma_{ij}^{\varepsilon}(x) = a_{ijkl}^{\varepsilon}(x) e_{kl}(\mathrm{u}^{\varepsilon}(x)), \tag{5}$$

$$e_{ij}(\mathrm{u}^{\varepsilon}(x)) = \frac{1}{2}(u_{i,j}^{\varepsilon}(x) + u_{j,i}^{\varepsilon}(x)), \text{ and} \tag{6}$$

$$\sigma_{ij}^{\varepsilon}(x)\mathrm{n}_j = 0 \quad \text{on } \partial\Omega_1 \quad \text{and} \quad u_i^{\varepsilon}(x) = 0 \quad \text{on } \partial\Omega_2 \tag{7}$$

where **u** is the displacement vector, $e_{ij}(\mathrm{u}^{\varepsilon}(\mathrm{x}))$ is the linearized strain tensor, $\sigma_{ij}^{\varepsilon}(\mathrm{x})$ denotes the stress tensor, $a_{ijkl}^{\varepsilon}(\mathrm{x})$ is the tensor of elasticity. Further, Eq. 8, Eq. 9, and Eq. 10 follow from the assumption that the mechanical response of the body is considered similar to the corresponding mechanical perturbation of the material properties of the body [43]; hence,

$$\mathrm{u}^{\varepsilon}(x) \equiv \mathrm{u}^0(x) + \varepsilon \mathrm{u}^1(x,y) + \varepsilon^2 \mathrm{u}^2(x,y) + \cdots \qquad x,y) \tag{8}$$

$$\sigma^{\varepsilon}(x) \equiv \sigma^{0}(x) + \varepsilon\sigma^{1}(x,y) + \varepsilon^{2}\sigma^{2}(x,y) + \cdots \qquad (x,y) \tag{9}$$

$$\mathrm{e}^{\varepsilon}(x) \equiv \mathrm{e}^{0}(x) + \varepsilon\mathrm{e}^{1}(x,y) + \varepsilon^{2}\mathrm{e}^{2}(x,y) + \cdots \qquad x,y) \tag{10}$$

Performing the chain rule as defined by Eq.11 while considering the assumptions from Eq. 8 to Eq. 10 in Eq. 4 to Eq. 6, the terms of different orders are separated. For equilibrium, same powers of ε are equated to zero. Further, after mathematical analysis as shown in [43], the constitutive Eq. 9 modifies to new constitutive Eq. 12, Eq. 13, and so on, given as,

$$\frac{\mathrm{d}}{dx_i} l = \left(\frac{\partial}{\partial x_i} + \frac{1}{\varepsilon}\frac{\partial}{\partial y_i}\right) l = l_{,i(x)} + \frac{1}{\varepsilon} l_{,i(y)} \tag{11}$$

$$\sigma_{ij}^{0}(x,y) = a_{ijkl}(y)\left(e_{kl(\mathrm{x})}(\mathrm{u}^{0}) + e_{kl(\mathrm{y})}(\mathrm{u}^{1})\right) \tag{12}$$

$$\sigma_{ij}^{1}(x,y) = a_{ijkl}(y)\left(e_{kl(\mathrm{x})}(\mathrm{u}^{1}) + e_{kl(\mathrm{y})}(\mathrm{u}^{2})\right) \tag{13}$$

…

Once the constitutive equation is formulated, the variational formulation of the asymptotic homogenization [43] may be numerically solved using the finite element software. Also, the macro stresses $\tilde{\epsilon}$, may be calculated by the volume average of Eq. 12. Thus, the effective constitutive equation for macroscopic scale is given Eq. 14,

$\tilde{\epsilon}$ $_{kl} e_{kl}(\mathrm{u}^{0})$, (14)

where a_{ijkl}^{h} is the effective material coefficients of the homogenized body. This approach was used to asymptotically homogenize the Nb_3Sn strands embedded in bronze matrix, which was further embedded in the copper matrix [43]. It was shown that the computed and the measured residual strains are in good agreement with each other [43].

2.2.2.2 Mean Field Approach

Mean field approach computes the microscopic stresses and strains in the RVE by the homogenization of the heterogeneous structure at the microscopic scale. Here, the homogenization refers to a method of conversion of the heterogeneous composite to a homogeneous material that has the same effective material properties when subjected to similar boundary conditions. For heterogeneous material, i.e. inclusion with different elastic properties than the matrix, the foundational framework of homogenization was provided by J.D. Eshelby.

In 1957, Eshelby [52] provided a solution for the constrained strain, $\varepsilon(\mathrm{x})$, for a single inclusion embedded in an infinite solid. The Eshelby solution approach consists of the following steps. First, from the considered infinite solid body with uniform stiffness C_o, an ellipsoidal inclusion with uniform stiffness, C_1, is removed and allowed to undergo the stress-free strain, E. Secondly, the strained inclusion is brought back to its original position with the application of a surface traction force and the inclusion is welded back in the initially removed cavity, which comprises of a surface, S. Thirdly, the traction forces on the composite body, spread over the surface is neutralized with the force of the same magnitude as that of surface traction force, over

surface *S*. The application of this force would free the body from external forces and make the body to undergo self-stress state caused by the transformation of inclusion.

Eshelby found that the stress-free strain is uniform for the ellipsoidal volume, (*I*), and is linked to the constrained strain, $\varepsilon(x)$, as [52],

$$\varepsilon(x) = \mathrm{B}^{\varepsilon}(I, \mathrm{C}_0, \mathrm{C}_1) : \mathrm{E}, \ \forall \mathrm{x} \in (\mathrm{I}), \tag{15}$$

where, B^{ε} is the strain concentration for the single inclusion and is given as,

$$\mathrm{B}^{\varepsilon}(I, \mathrm{C}_0, \mathrm{C}_1) = \left\{ I + \zeta(I, \mathrm{C}_0) : \mathrm{C}_0{}^{-1} : [\mathrm{C}_1 - \mathrm{C}_0] \right\}^{-1} \tag{16}$$

where $\zeta(I, \mathrm{C}_0)$ is the Eshelby's tensor.

Similarly, further developing the approximate Eshelby solution, Mori-Tanaka in 1973 [53] provided the homogenization of the multi-inclusion problem. Physically this model assumed that the field in a particular inclusion in a multi-inclusion matrix is independent of the field due to its neighboring inclusions. Now, provided the local analysis is complete, the macroscopic (average) stress, $\bar{\sigma}_{ij}$, and macroscopic strain, $\bar{e}_{ij}$, may be computed by integrating the local stress and local strain over the volume, *V*, of the body, using Eq. 17 and Eq. 18.

$$\bar{\sigma}_{ij} = \frac{1}{V} \int_V \sigma_{ij} dV \tag{17}$$

$$\bar{e}_{ij} = \frac{1}{V}\int_V e_{ij} dV \tag{18}$$

Though the above homogenizations models may be solved numerically, they do not consider the effect of microstructural features such as porosity, shape, size, and orientation of the particle phase in the composite on the macroscopic response of the material.

Another material model providing the macro-stress state of the MMC with the incorporation of microstructural features is the Gurson model, developed in 1977 [54, 55]. The Gurson model is used to predict the ductile failure of the material. The ductile failure is due to the microvoid nucleation and growth, which in model is controlled by the user defined nucleation parameter and geometry of void. Figure 10 shows the graphical representation of the RVE consisting of the ellipsoidal void. In the Gurson model, these voids are assumed to be spherical and they do not undergo shape change in the analysis. Though, the model considers the microvoid nucleation and growth, it may not predict the coalescence of the voids. This is due to the assumption of homogeneous deformation of the material. In addition, the amount and onset of the nucleation of voids in Gurson model is a user input parameter [55]. Further, according to Zhang, *et al.* [55], for a strain-controlled experiment, the nucleation rate of voids may be given as Eq. 19 and during plastic deformation, growth rate of voids is computed as Eq. 20,

$$\mathrm{d}f_{\text{nucleation}} = f_{\varepsilon}(\bar{\varepsilon}^{\mathrm{p}})\mathrm{d}\bar{\varepsilon}^{\mathrm{p}}, \tag{19}$$

where

$$\mathrm{d}f_{\text{growth}} = (1-f)\mathrm{d}\varepsilon^{\mathrm{p}} : \mathrm{I}, \tag{20}$$

where f_ε is the void nucleation intensity, and $\bar{\varepsilon}^{p}$ is the equivalent plastic strain during plastic deformation, ε^{p} is the plastic strain and I is the second order unit tensor. The theoretical framework for the derivation of the constitutive equation [55], Eq 21, is provided in [49, 56].

$$\phi(q,\bar{\sigma},f,\sigma_{M}) = \frac{q^2}{\bar{\sigma}^2} + 2q_1 f \cosh\left(\frac{3q_2\sigma_{M}}{2\bar{\sigma}}\right) - 1 - (q_1 f)^2 = 0 \tag{21}$$

where f is the void volume fraction, σ_{M} is the mean normal stress, q is the conventional von Mises equivalent stress, $\bar{\sigma}$ is the flow stress of the matrix material, and q1 and q2 are constants.

To consider the effect of shape change and rotation of the voids for elasto-plastic porous materials, the constitutive models like variational (VAR) and modified variational (MVAR) [49, 56] are available. The detailed derivation of the constitutive equation for the MVAR is derived in [56]. It was shown that the prediction of the microstructural evolution (void volume, aspect ratio, and void rotation) for an elasto-plastic porous material is in good agreement with the tensile test data results of a high strength steel [56].

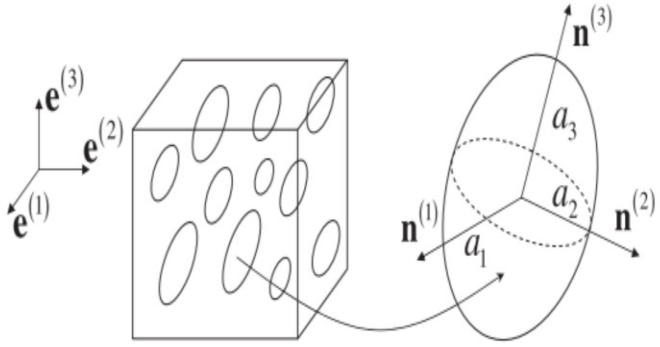

Figure 10: Graphical representation of the RVE consisting of the ellipsoidal void with a_1, a_2 and a_3 as the semi-axis [55].

In general, various attempts to simulate the quasi-static response of particle reinforced composites were made in the past and readers are directed to [42–50, 56]. In most of these models, the two phases of the composite are treated separately with the assumption of perfect interfacial bonding. However, as stress fields interact at the level of the microstructure [57–60] and as noted by most of the researchers [43,45, 47, 57–60], interface decohesion is one of the primary failure modes in MMC materials. So, to incorporate the effect of interface decohesion, the interface may be modelled using cohesive elements [47, 59, 60]. In theory, these cohesive elements circumscribe the reinforcement with a user-defined thickness. So, instead of assuming a perfect bonding between the particle and the reinforcement, Finite Element software enable the definition of a failure criteria for these cohesive elements. These failure criteria may be based on either critical stress or critical strain [45, 47]. Although the advancement of this approach is promising to model the interface, it is restrained due to lack of availability of the interfacial mechanical properties. Huang, *et al.* [45] have explored this by either assuming the average of mechanical properties of MMC constituents or by varying the mechanical property values ranging between the constituent's properties for the cohesive elements. Based on available literature [45], it may be inferred that a high elastic modulus of cohesive elements favours the fracture of the interface while a low elastic modulus of cohesive elements leads to a significant strain of the RVE.

In 2014, Holmberg, *et al.* [33] reported the computational wear model for the thermal sprayed WC-CoCr coatings and laser cladded WC-NiCrBSi coatings. The modelling results were achieved by three different models. First, to understand the general material behaviour, the synthetic model was defined. This model was characterized by the ideal microstructure such that

there were no defects in the material. The computational analysis from a synthetic model may represent the baseline of the material performance. Second, defects such as porosity, voids, and pre-existing cracks were introduced in the synthetic model and the interaction in defects was considered in what they named as the advanced synthetic model. Third, to obtain the stress-strain response under the actual loading, SEM images were discretized and coupled with constitutive equations to solve the formulation; method coined as the real image method. Table 1 shows that for the thermally sprayed WC-CoCr coatings, defects such as porosity and cracks have the most deterimental effect on the wear resistance of the coating as it may lead to the earlier onset of the failure. Also, matrix elasticity was shown to be least effecting the wear of the modelled coating. Further, Holmberg, *et al.* [32, 33] reports that for an indentation test, the developed micromechanical model was in good correlation with the experimental data; however, the results of the virtual scratch test were not in an agreement with the actual scratch test results. As noted by Holmberg, *et al.* [32, 33], this deviation is explainable as the model does not consider the effect of material detached from the contact surface and the effect of surface roughness during the scratch test. This suggests that to effectively simulate the dynamic wear problem the following simplifications are to be minimize.

For simulating the mechanical response of the MMC coatings, several assumptions are made in microstructure such as simplifying the shape and orientation of the particles to make the analysis simple and computing efficient [40]. According to [36, 61], the realistic wear simulation needs to consider the three bodies boundary condition in the model. Unlike two bodies, where abrasive particles only roll over the surface, in three bodies, the abrasive particles roll as well as cut the surface. Thus, three bodies wear problem formulation includes more variables and is in

general challenging to model. Also, Abedini, *et al.* [48] notes that while the MMC is under experiment, the load carrying capacity of the removed carbide does not go to zero, as assumed by [31, 40], instead cracked particles absorbs the load from the matrix. These assumptions in the formulation of mechanical response under various loading conditions demand more research to further look into the sources of uncertainty and phenomenon to be explained by new and better models.

Extensive studies and research activities have been conducted on the modelling of mechanical properties and performance of particle reinforced metal matrix composite coatings [31–33, 42–51]. Initially most of the research on how different constituents of the composite impacts the performance was focused only on experiments and researchers proposing the theories of effective bounds of the selected material property [31, 37–39]. However, with the advancements in computing technology, it is now possible to virtually generate both 2-D as well as 3D microstructures [32, 33]. These models with different model sizes and tailored microstructural features may be solved numerically [32, 33, 40]. Although researchers have shown that simulations are time efficient and lead to better prediction of mechanical response of MMCs, the models are still far from the correct representation of the wear problem to incorporate the contact and boundary conditions.

Table 1: Effects of coating properties and microstructural features on the mechanical behaviour and wear resistance. The "+" symbols represent the relative weight of each parameter [32].

	Effect on stresses	**Effect on strain**	**Comment**
Matrix elasticity	+	+	Considering matrices able to deform
Matrix hardness	++++	+++++	Considering matrices able to deform
Particle elasticity	+++++++	+	Assuming particle elasticity greater than matrix
Particle hardness	+++	++	Assuming particle elasticity greater than matrix
Particle size	+++	+++	In the investigated range
Particle morphology	+++++	++++	Imaging derived results-based conclusion
Particle clustering	++++++	++++++	Effect can be local
Mean free path	++++	++++	-
Porosity*	+++++	+++++	Effect can be local
Defects*	++++++++	+++++++	Effect can be local

*Defect=crack, porosity with very high aspect ratio.

2 Experimental Method

2.2 Feedstock powder and substrate

To fabricate the MMC coatings, a mechanical blend of three different powders was prepared. The selection of the constituents of the feedstock powder was based on wear resistance characteristics of the final coatings. Melendez, *et al.* [26] and Lee, *et al.* [28] have already shown that the wear resistance of the cold sprayed WC-Ni was remarkable. Therefore, commercially available Ni (N5001, CenterLine Ltd., Windsor, ON, Canada) powder was selected as the powder to form the metal matrix and WC (WC-8245, Pacific Particulate Materials Ltd., Port Moody, BC, Canada) powder for the hard-reinforcing phase. The size distribution of the as-received Ni powder was -45+5 μm (5 to 45 μm), and that of WC was -270 mesh (-53 μm). Figure 11 and Fig. 12 shows the morphology of the powder particles. As observed from Fig.11, the WC particles are angular with sharp edges, and Ni particles are highly dendritic in structure (see Fig. 12).

To maintain the quality and reproducibility of the coatings, the powders were deposited on the substrates as used by Lee *et al.* [28], i.e., low carbon steel. The roughness of the substrate is an important factor determining the adhesion strength between the coating and the substrate [13, 21]. Therefore, prior to the deposition of feedstock powder, the low-carbon steel substrates were grit-blasted using the grit blaster. An alumina-based abrasive media (#24 alumina grit, Manus Abrasive Systems Inc., Edmonton, AB, Canada) was fed to the grit blaster at a 90-psi pressure provided by the building system.

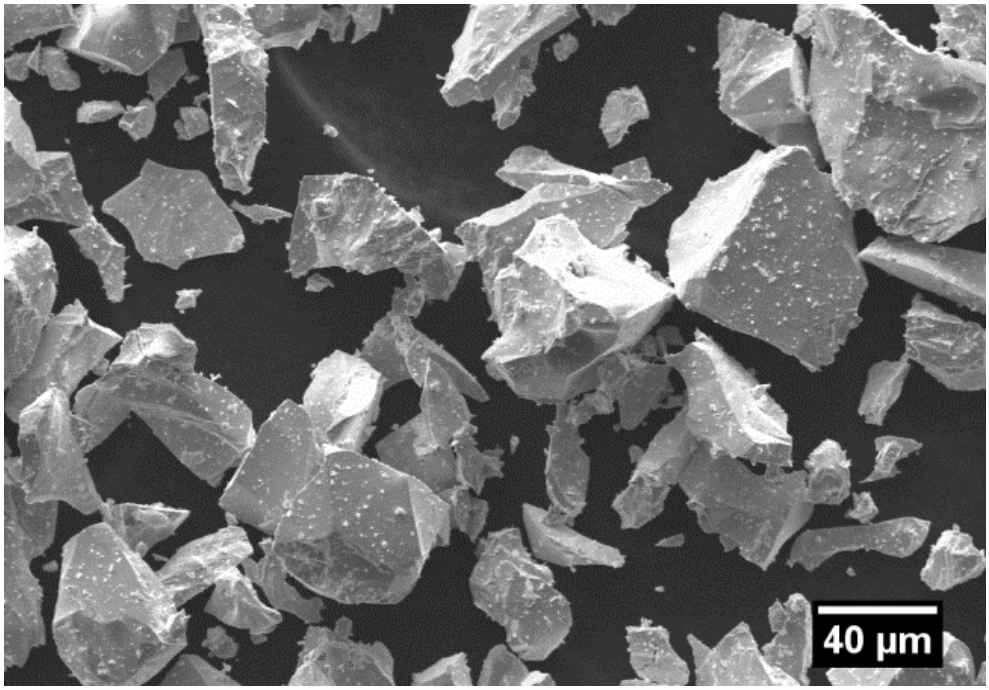

Figure 11 SEM image of powder morphology of WC [28]

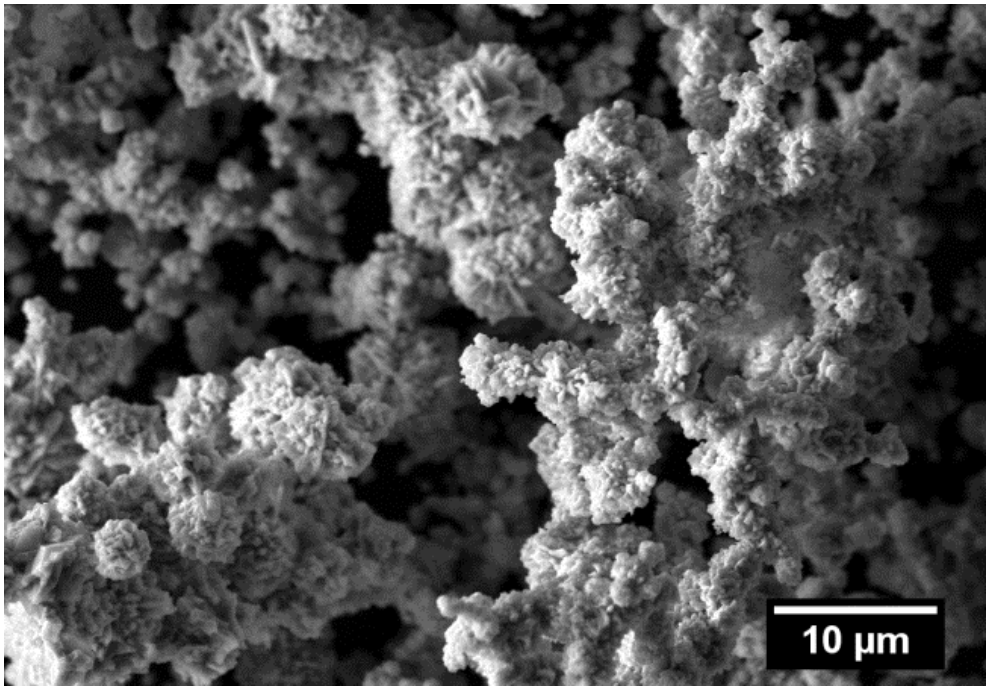

Figure 12 SEM image of powder morphology of Ni [28]

2.3 Cold spray deposition

The prepared feedstock powder was fed to a low-pressure cold spray system (SST series P, CenterLine, Ltd., Windsor, ON, Canada) to deposit the powder on the substrate. To accelerate the feedstock powder, compressed air at 634 kPa was used as the working fluid. The cold spray gun was mounted on an automatic robot (HP-20, Motoman, Yaskawa Electric Corp., Waukegan, IL, USA) to enhance the powder deposition quality and achieve repeatability in coating fabrication (see Fig. 13). The use of the robot ensured a constant stand-off distance between the spray nozzle and the substrate. The robot was programmed to raster in the linear direction with a fixed increment in the in-plane perpendicular direction at the end of the substrate. The cold spray system parameters for the powder deposition parameters were selected from the previous work of Lee, *et al.* [28]. These parameters are summarized in Table 2.

Table 2: Cold spray deposition parameters

Process Parameter	**Value**
Process Gas	Compressed air
Compressed Air Pressure	634 kPa
Compressed Air Temperature	550°C
Stand-off Distance	5 mm
Nozzle velocity	5 mm/s

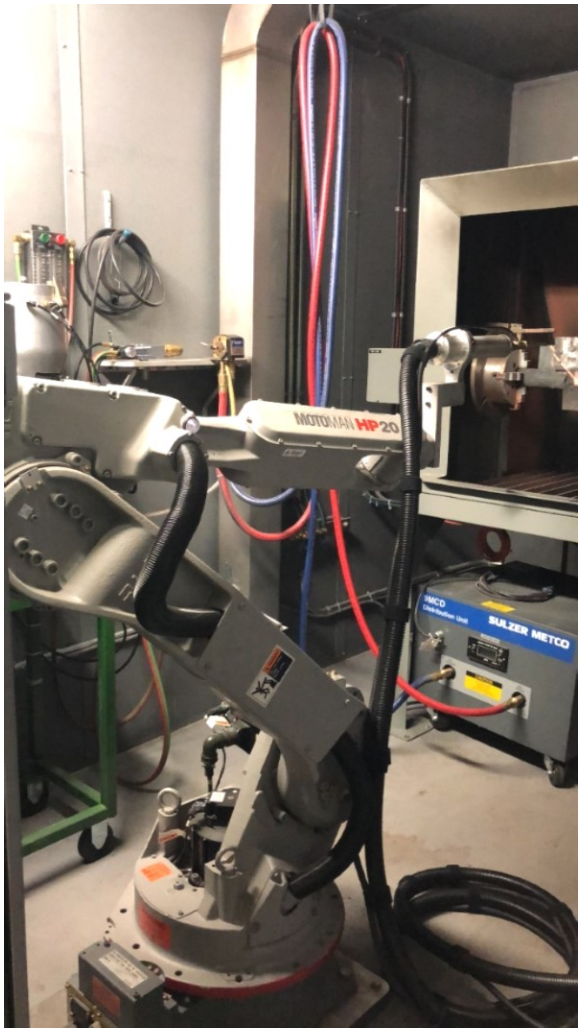

Figure 13 Cold spray gun mounted on the HP-20 Motoman robot

2.4 Coating characterization

To conduct the microscopic diagnostic of the coatings, the cross-sectioned coating samples were cold-mounted in an epoxy resin (Allied High Tech Products, Inc., Rancho Dominguez, CA, USA). The prepared epoxies were grounded using the 240, 360, 400, 800, and 1200 grit silicon carbide paper (LECO, Mississauga, ON, Canada) and further polished using 3 µm and 1 µm

diamond slurries (LECO, Mississauga, ON, Canada). Scanning electron microscopy (EVO 10, Zeiss, Cambridge, UK) was used to characterize the microstructure of the coatings. The SEM was operated with the acceleration voltage set at 20 kV and a working distance of about 7 mm.

The captured images from the SEM were used to characterize the WC particle content, porosity, particle-matrix interfacial area, average particle size, and mean free path between the reinforcing particles in the coatings. These measurements were facilitated by the ImagePro software (ImagePro, Media Cybernetics, Bethesda, MD, USA). To calculate the WC particle content in the coatings, a built-in function (Count) in ImagePro software was used. The count function identifies WC particles as entities that are brighter or darker than a set intensity. The count function estimates the area of the WC particles, which was further used to estimate the vol.%.

The micrographs were utilized to measure the mean free path between the reinforcing WC particles, which is illustrative of the distance between the nearest WC particles. The mean free path was determined by utilizing Eq. (22), defined as, [64]

$$\lambda = \frac{1 - v_r}{N_L}. \tag{22}$$

where v_r is the volume fraction of the reinforcing WC particles and N_L is the number of particle intercepts per unit length. To calculate N_L, five different lines were drawn on the SEM image and number of particles intercepted with the drawn lines were manually counted. The average particle size of the reinforcing WC particles was appraised using the in-built function (Area

(polygon)) in ImagePro software. The average size of the particle was estimated by calculating the average size of at least fifty particles per area of interest. Thus, the standard deviation in the data of average particle size shows the standard deviation of the average of particle size instead of the standard deviation of particle size. The particle-particle interfacial area was calculated using the in-built function (Perimeter) in ImagePro software. For all the calculations of the microstructure, at least five SEM images were studied with at least five areas of interest per SEM image (n = 25).

2.5 Digital image correlation

In this study, the strains in the tensile specimens were computed using the DIC technique [65, 68]. Considering this technique novel in the field of coatings, a summary is provided here. To perform DIC and calculate the strain fields, an *in-situ* capturing of the deformation of the samples was done using a Promon U750 High Speed Camera (AOS Technologies AG, Taefernstrasse 20 CH-5405 Baden-Daettwil, Switzerland). The video was recorded at 100 frames/s and full resolution of 1280 × 1024 pixels. The recorded video was utilized to obtain the time stamped images and were loaded in the DIC software, Vic 2D 6 [67]. To generate reliable data from the DIC, a high-quality speckle pattern is a prerequisite. To generate the speckle pattern on the specimens, an ultra-fine Harder and Steenbeck Infinity airbrush was used. The diameter of the spraying needle was 0.15 m. The quality of the speckle pattern is shown in Fig. 14 (a) and as observed; the speckle pattern is highly contrasted. This quality was also evident from the Vic 2D software, where the computer suggested subset size was between 15 × 15 and 25 × 25 pixels. To achieve this high contrast, high intensity LEDs were used to obtain high brightness. In the

software, an area of interest (AOI) is defined on the specimen for which strain fields are to be calculated (see Fig. 14 (b)). The AOI is further subdivided into smaller areas called subsets. These grids formed by the subsets is then digitally tracked by the software in the subsequent time stamped images of the experiment [68]. The failure strain as calculated from the DIC is then matched with the failure stress from the MTS machine and then all the corresponding tensile stresses and strains are reconciled to obtain the final tensile stress-strain curves.

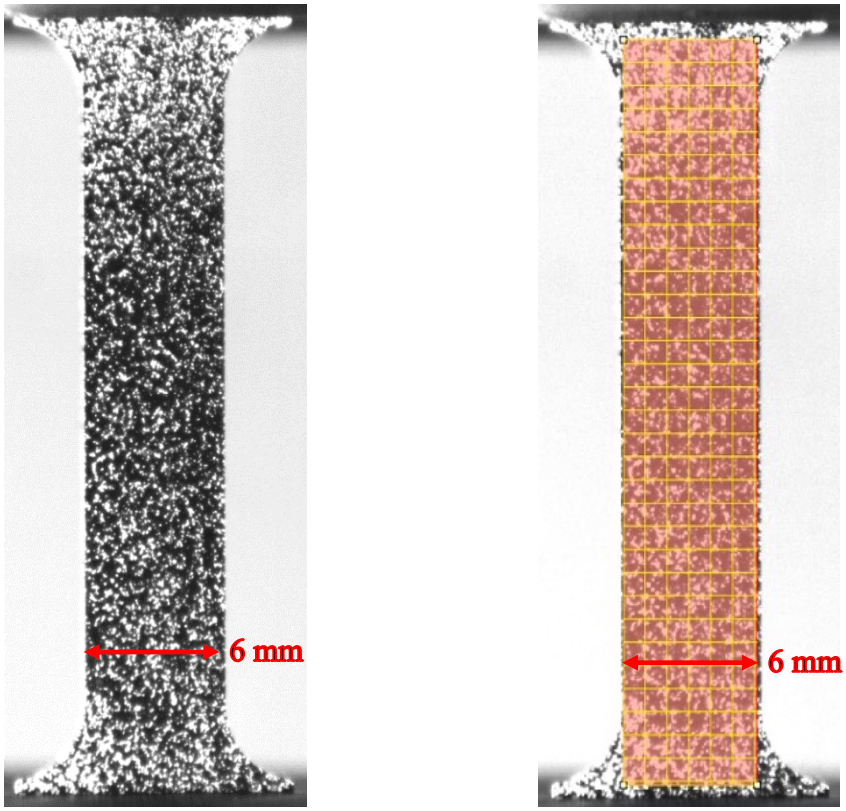

(**a**) (**b**)

Figure 14: (**a**) Image presenting a typical speckle pattern on the surface of the tensile specimen. (**b**) Image showing the AOI for which the average axial strains and lateral strains were calculated. Each smaller square in the AOI represent the subset of the grid, which was digitally tracked by the Vic 2D.

2.6 Tensile testing

The tensile testing was conducted on the Material testing system (MTS 810, MTS Systems Corporation, Minneapolis, MN, USA) located in the machine shop of the Department of Mechanical Engineering at the University of Alberta (see Fig. 15). Prior to tensile testing, tensile test coupons were prepared from the fabricated WC-Ni MMC coatings (see Fig. 14). This was accomplished by cutting the coating samples using a wire-based electrical discharge machine (Agie Progress V4, Agie, 1242 Satigny, Switzerland). The gauge dimensions of the samples (25 mm × 6 mm × 1.2 mm) were prepared according to the ASTM Standard E8/E8M-13a [69]. The standard advises the minimum dimensions that are required to generate the plane strain condition in the samples undergoing tensile loading. The tensile specimens were loaded in the quasi-static regime at a loading rate of 0.001 mm/s.

Figure 15: Image of the MTS machine that was used to conduct the tensile tests. The arrow shows the Promon U750 high speed camera that was used to capture the deformation video to be used as an input to DIC.

3 Results and Discussions

The focus of this thesis was to quantify and assess the mechanical properties of cold-sprayed WC-Ni MMC coatings. The effect of WC wt.%, particle-matrix interfacial area, particle-particle mean free path, average particle size, and porosity of the coating on the tensile strength and Young's modulus of the coating was also explored. Further, mechanical energy absorbed to failure and damage in the coatings was quantified and used to explain the significant improvement of the coatings consisting of the content of WC beyond 30 wt.%.

In this chapter, the results are presented in the following order: 1. Characterisation of the WC-Ni coatings fabricated by the cold spray; 2. Tensile stress-strain response of the cold sprayed coatings, including the Young's modulus, the tensile strength, the strain to failure, and the toughness of the coatings; 3. Exploration and discussion of the observed phenomenon of the strengthening of MMC with an increase in the content of WC wt.% and refined microstructure. This chapter also explores the preliminary results of modelling the tensile mechanical response of the tested coatings.

3.2 Deposition of cold-sprayed WC-Ni powder

Figure 16 shows the cross-section of the successfully deposited feedstock powder. The feedstock powder comprises of three different powder blends of WC and Ni, based on the 50, 71, and 92 wt.% of WC. For the identical coatings that were fabricated by Melendez, *et al.* [26] and

Lee, *et al.* [28], they noted that the bright objects in the Fig. 16 corresponds to the deposited WC particles while the darker area corresponds to the Ni metal matrix. As observed in Fig. 16, with an increase in the content of WC wt.% in the feedstock powder from 50 wt.% to 92 wt.%, there is an increase in the content of WC in the coating as well (compare Fig. 16 (a) and Fig. 16 (c)). The increase in the content of WC in the coating was further confirmed from the calculated wt.% in the coating from the image analysis. This was plotted and shown in Fig. 17. The calculated data confirm that with an increase in content of WC wt.% in the feedstock powder, there is an increase in the content of WC wt.% in the coating. For example, WC wt.% increases from approximately 6 wt.% to 35 wt.% in the coating as the WC wt.% in the powder blend increased from 50 wt.% to 92 wt.%. This is because, with an increase in WC wt.% in the powder blend, a greater number of particles impinge the substrate and previously deposited layers and hence more WC gets deposited and embedded in the metal matrix [12, 19, 20]. Further, Fig. 16 suggests that the distribution of the reinforcing particles in the metal matrix is heterogeneous as they are non-uniformly distributed in the metal matrix. This is due to the characteristic of cold spraying process by which the composites were prepared. Due to the inherent non-uniformity in the acceleration of particles in the cold spray process, the impinging particles bond to the substrate at random locations and hence produce the heterogeneity. This was also noted by Lee, *et al.* [28] while fabricating the cold spray WC-Ni MMC coatings.

However, Fig. 17 also indicate that a lower WC wt.% got deposited in the coating than present in the initial feedstock powder blend. For example, approximately 35 wt.% of WC was deposited when 92 wt.% of WC was in the powder blend (see Fig. 17). Irissou, *et al.* [12] explained this phenomenon by considering that the hard WC particles do not deform plastically

on their impact with the substrate and hence their inability to adhere to the substrate. Thus, a lower amount of WC, which is entrapped by the Ni particles is retained in the coating. This was also confirmed by Lee, *et al.* [28].

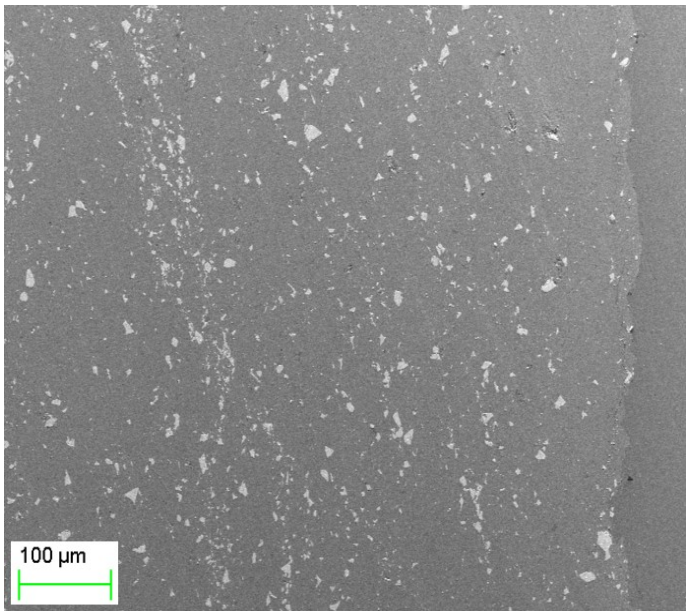

(*a*)

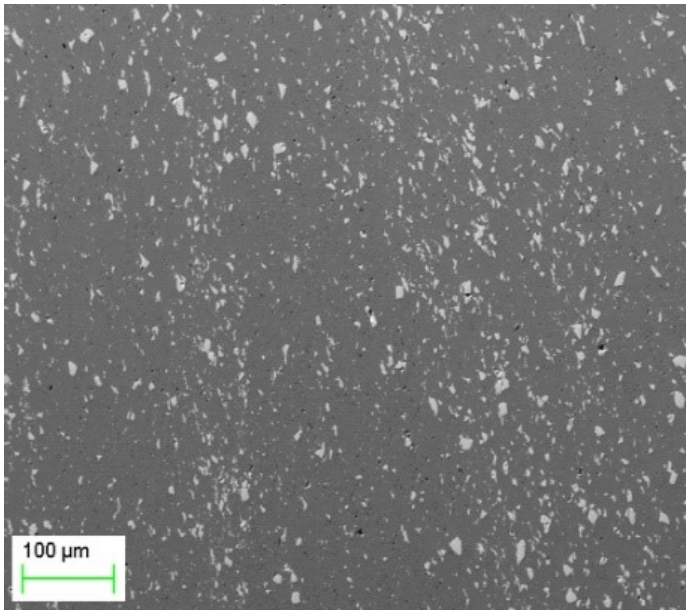

(*b*)

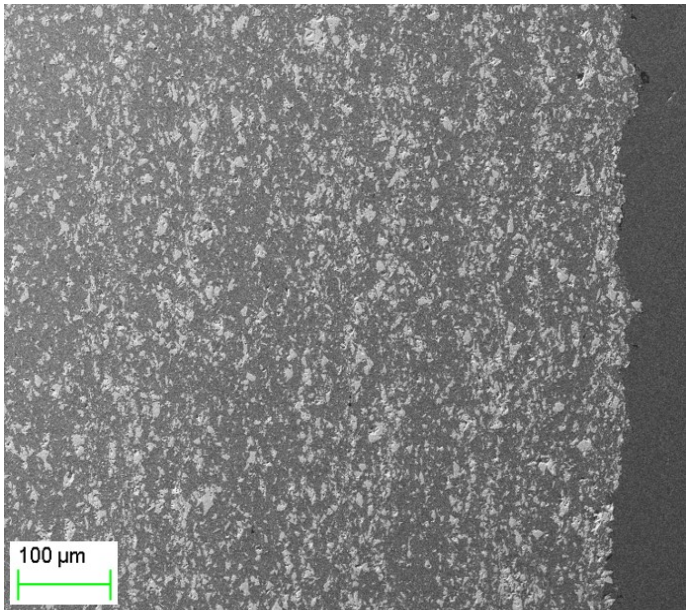

(*c*)

Figure 16 Cross-sectioned SEM images of the fabricated MMC coatings with powder blend of (*a*) 50 wt.% WC + 50 wt.% Ni, (*b*) 71 wt.% WC + 29 wt.% Ni, and (*c*) 92 wt.% WC + 8 wt.% Ni.

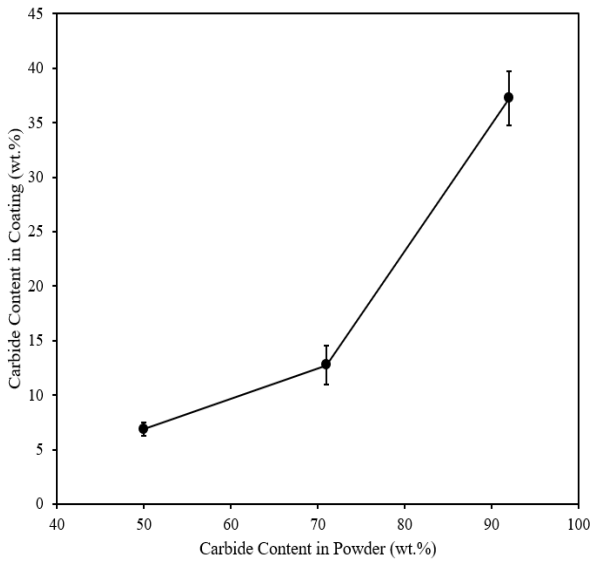

Figure 17 Curve of reinforcing WC particle content in the coating versus WC particle content in the feedstock powder (weight percentage).

3.3 Tensile testing

Figure 18 shows the tensile stress-strain curves for the tested cold sprayed WC-Ni MMC coatings. The content of WC wt.% in these coatings varies from approximately 6 wt.% to 40 wt.%. The legend shows the corresponding content of WC as the wt.% in the coating. The slope of the curves in Fig. 18, which is equivalent to the Young's modulus, was determined by calculating the slope of the curves at approximately 0.016% strain. Table 3 documents the calculated values of the Young's modulus. Table 3 indicates that Young's modulus of the tested coatings increases with an increase in the content of WC in the coatings. A similar trend was also observed for the tensile strength, the failure strain, and the mechanical energy absorbed to failure of the coating, which is equivalent to toughness. The mechanical energy that was absorbed to failure was determined by calculating the area under the obtained tensile stress-strain curves (see Fig. 18). Numerous scientists have likewise noted an improvement in the mechanical properties with an increase in the content of the reinforcing phase in the MMC [9, 22, 26, 32, 33, 36–40, 70–72]. They attributed this improvement to refinement in the microstructure of MMCs with an increase in the reinforcing phase [9].

As detailed in Chapter 2 of this thesis, similar to the approximation of effective hardness of the composite, the first approximations of the Young's modulus of the cold-sprayed WC-Ni MMC coatings may be calculated by assuming either iso-strain condition per the Voigt model (Eq. 1a, Upper bound) or iso-stress condition per the Reuss model (Eq. 1b, Lower bound) [15, 44]. Using the bulk material Young's modulus of Ni and WC as 220 GPa [17] and 691 GPa [83], respectively; the estimated Young's modulus of cold-sprayed WC-Ni MMC coatings is shown in

Table 3. Table 3 indicates that the experimental Young's modulus is outside the bounds as predicted using the Eq. 1a and Eq. 1b. For example, the predicted Young's modulus for 37.78 ± 0.04 wt.% WC coating is between 266 GPa to 340 GPa. However, a lower value of Young's modulus of 247 GPa was observed experimentally. The lower value of experimental Young's modulus may be due to the characteristic of the cold spray fabrication process or the deviation as explained by Chawla, *et al.* [9] and Lee, *et al.* [31]. They attributed the deviation to the simplicity of the physics in these equations and the inability to incorporate the microstructure of the composites [9, 31]. Chawla, *et al*. [9] have demonstrated that microstructural features, for example, shape, size, particle-particle mean free path, and many others in an MMC fundamentally influence the full-scale mechanical response of the composites. According to Lee, *et al.* [31] these estimations do not consider the effect of constituent's fracture toughness and particle-matrix interfacial properties, recognized to influence the overall mechanical properties of the composite.

Gustafson, *et al.* [74] and Lee, *et al.* [75] noticed that the particle-particle mean free path impacts the yield strength of the MMC. Likewise, Kouzeli, *et al.* [64] showed a critical improvement in the hardness of MMC coatings that had particle-particle mean free path under 10 μm. This was also affirmed by Hodder, *et al.* [24] who demonstrated that for Al_2O_3 reinforced MMC coatings, a reduction in mean free path, augmented with dislocations, brings about higher hardness estimations of low-pressure cold sprayed coatings. Further, the impact of grain size on the strengthening of metals and failure of brittle materials have been considered extensively, and connections, for example, the Hall-Petch and Griffith criteria have demonstrated that the strength of metal increments with a diminishing in the grain size of the metal [76]. Hence, the impact of

microstructure on material and mechanical properties of multiphase materials is broadly recognized and is one of the primary perspectives in the designing of MMCs with improved performance. An essential and comprehensive understanding of the mechanical behaviour of cold sprayed coatings under external loading and the association between the microstructure of the coating and the mechanical behaviour is yet deficient. Therefore, the strengthening of cold sprayed WC-Ni MMC coatings with an increase in the content of WC wt.% and refinement in the coating microstructure is detailed further.

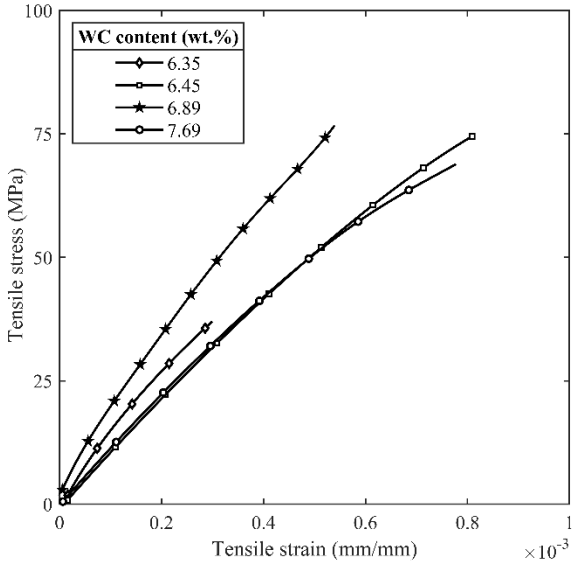

(*a*)

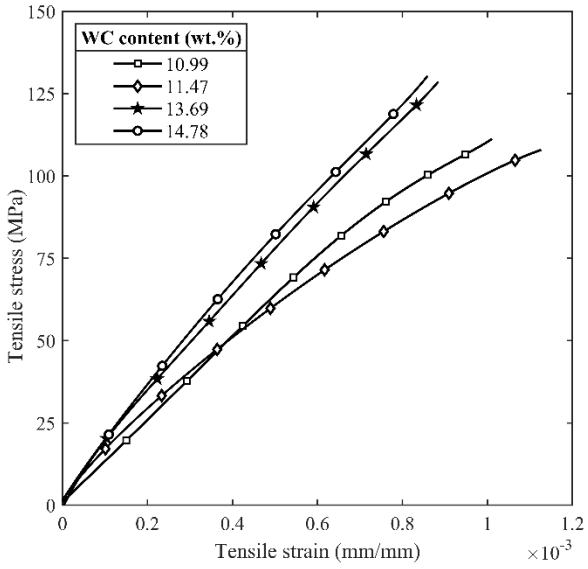

(*b*)

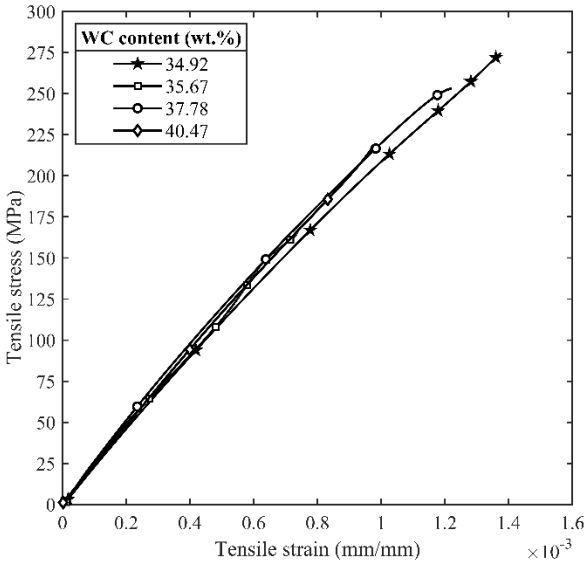

(*c*)

Figure 18: Tensile stress-strain curves of the cold-sprayed MMC coatings fabricated from (*a*) 50 wt.% WC + 50 wt.% Ni powder blend, (*b*) 71 wt.% WC + 29 wt.% Ni powder blend, (*c*) and 92 wt.% WC + 8 wt.% Ni powder blend. The final wt.% of the reinforcing WC particles in the coating is as indicated on the plot.

Table 3: Mechanical properties of the cold sprayed WC-Ni MMC coatings- Young's modulus, tensile strength, failure strain, and toughness.

wt.% WC in coating (n = 25)	Young's modulus (Experimental) (GPa)	Young's modulus estimation (Lower bound – Upper bound) (GPa)	Tensile strength (MPa)	Failure strain (%)	Toughness (N/mm^2)
6.35 ± 0.06	121	226 – 238	37.91	0.036	0.006
6.45 ± 0.11	114	226 – 237	71.84	0.082	0.033
6.89 ± 0.05	133	226 – 239	76.86	0.084	0.023
7.69 ± 0.07	116	227 – 243	68.52	0.079	0.03
10.99 ± 0.07	123	230 – 251	110.76	0.101	0.062
11.47 ± 0.04	137	231 – 252	109.82	0.113	0.071
13.69 ± 0.03	152	233 – 259	127.76	0.089	0.061
14.78 ± 0.04	150	234 – 262	130.95	0.086	0.06
34.92 ± 0.03	233	261 – 329	276.09	0.140	0.199
35.67 ± 0.05	210	263 – 332	168.15	0.092	0.063
37.78 ± 0.04	247	266 – 340	256.83	0.123	0.167
40.47 ± 0.03	235	271 – 350	220.11	0.101	0.109

3.4 Effect of WC content in the coating on mechanical properties

The reinforcing particle content in MMC coatings affects their tensile strength [9]. With an increase in the content of reinforcing particles in the metal matrix, the tensile strength of the

MMC increases. Researchers have explained this strengthening of MMC to the fact that the MMC that has more particles, it can transfer the more external load to the stiffer carbide than the MMC with a smaller number of particles [9]. This has also been used to explain the increase in hardness of WC-Ni MMC coatings by Lee, *et al.* [28].

In this study, the effect of reinforcing particle content on the tensile strength of cold sprayed WC-Ni MMC coatings was studied by quantifying the total interfacial area (Ψ) between the WC reinforcing particles and the metal matrix. From the definition of Ψ, it constitutes the area that was available to share and transfer external load from the metal matrix to the stiffer carbide. Figure 19 presents the plot of tensile strength as the function of Ψ. As observed for Fig. 19, with an increase in Ψ, there is an increase in the calculated tensile strength of the coating. For example, a coating containing 6.45 ± 0.11 wt.% WC had a total interfacial area per unit thickness of approximately 8253 ± 133 μm^2, while a coating containing 35.67 ± 0.05 wt.% WC had a total interfacial area per unit thickness of approximately 30001 ± 2774 μm^2. Further, the trendline in Fig. 19 suggests that there is a direct relationship between the tensile strength and Ψ, which is functionally shown in Eq. (23) as,

$$\sigma \propto \psi \,. \tag{23}$$

The Eq. (23) is vital in proving the proposed structure of strengthening of the cold sprayed WC-Ni MMC coatings by the load sharing mechanism. Thus, the increase in the tensile strength of cold sprayed coatings conforms with the concept of distribution of external load from the metal matrix to the stiffer carbides embedded in the matrix.

Table 4: Microstructural features of the cold sprayed WC-Ni MMC coatings- total interfacial area, mean free path, average reinforcing particle size, and porosity.

wt.% WC in coating (n = 25)	Total interfacial area (μm^2) (n = 25)	Mean free path (μm) (n = 25)	Average reinforcing particle size (μm^2) (n = 25)	Porosity (%) (n = 25)
6.35 ± 0.06	5586 ± 147	83 ± 10	19.37 ± 0.44	0.48 ± 0.03
6.45 ± 0.11	8253 ± 133	75 ± 10	19.27 ± 0.48	0.35 ± 0.03
6.89 ± 0.05	8273 ± 209	79 ± 9	18.02 ± 0.30	0.41 ± 0.02
7.69 ± 0.07	7018 ± 214	54 ± 6	18.33 ± 0.7	0.34 ± 0.03
10.99 ± 0.07	9901 ± 128	42 ± 5	13.27 ± 0.34	0.45 ± 0.11
11.47 ± 0.04	9867 ± 115	44 ± 6	14.54 ± 0.35	0.42 ± 0.06
13.69 ± 0.03	10032 ± 129	38 ± 4	11.84 ± 0.27	0.30 ± 0.03
14.78 ± 0.04	11922 ± 196	36 ± 4	12.17 ± 0.31	0.32 ± 0.02
34.92 ± 0.03	42834 ± 3960	13 ± 0.4	7.24 ± 0.31	0.037 ± 0.004
35.67 ± 0.05	30001 ± 2774	15 ± 0.8	9.03 ± 0.16	0.048 ± 0.001
37.78 ± 0.04	37106 ± 9811	12 ± 0.4	8.64 ± 0.29	0.042 ± 0.005
40.47 ± 0.03	35524 ± 3960	13 ± 0.2	9.19 ± 0.33	0.049 ± 0.006

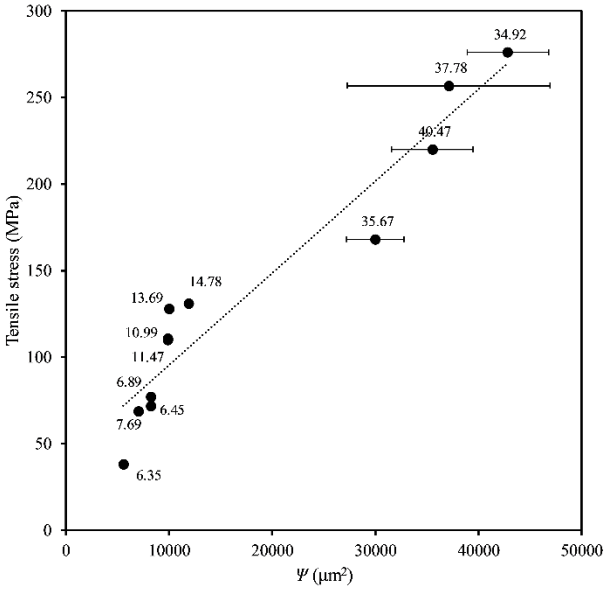

Figure 19 Tensile strength of cold sprayed MMC coatings versus the total interfacial area per unit thickness (Ψ) between the WC particles and the metal matrix. The wt.% of the WC particles in the coating is indicated on the plot.

3.5 Effect of particle-particle mean free path on mechanical properties

The mean free path in the MMC coatings affects their mechanical property [24, 64]. The effect of the mean free path was studied in detail by Hodder, *et al*. [24] and Melendez, *et al.* [26] for the cold sprayed WC-Ni MMC coatings. They reported an increase in hardness of the coating with a decrease in the particle-particle mean free path in the coating [24, 26]. Their framework motivated to investigate the effect of λ on the tensile strength of the cold sprayed coatings as well. Table 3 and Table 4 suggest that with an increase in the content of WC wt.% in the coating, the mean free path decreases. For example, for a coating containing 6.35 ± 0.06 wt.% WC, the mean free path is 83 ± 10 μm, compared to mean free path of 13 ± 0.4 μm at 34.92 ± 0.03 wt.%

WC in the coating. Further, Gustafson, *et al.* [74] and Lee, *et al.* [75] likewise examined the impact of λ on the strength of the composites. They depicted a useful connection between the strength and λ and revealed a straight increment in strength as a function of $\frac{1}{\sqrt{\lambda}}$, or in equation form as,

$$\sigma \propto \frac{1}{\sqrt{\lambda}} \tag{24}$$

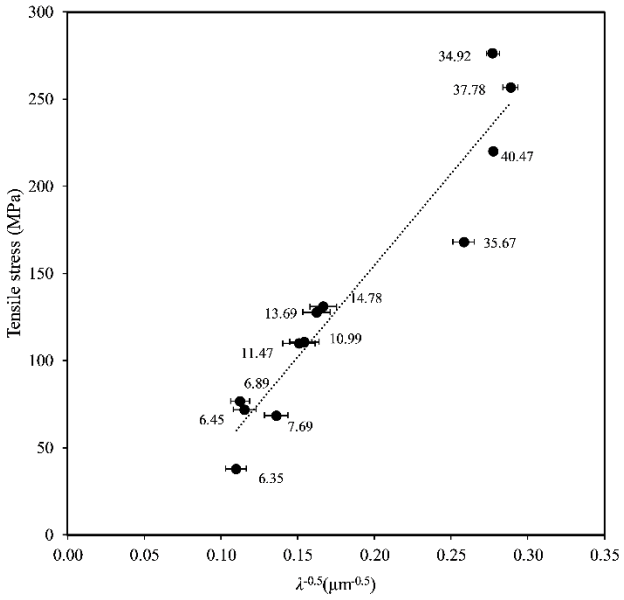

Figure 20: Tensile strength of cold sprayed MMC coatings versus the inverse square root of the particle-particle mean free path. The wt.% of the WC particles in the coating is indicated on the plot.

For the cold sprayed WC-Ni coatings tested in this study, the tensile strength as a function of $\frac{1}{\sqrt{\lambda}}$ is shown in Fig. 20. Figure 20 indicates great concurrence with the proposed structure as it demonstrates an almost straight connection between the tensile strength of the as-sprayed MMC coatings and $\frac{1}{\sqrt{\lambda}}$. An increase in tensile strength with a decrease in particle-particle spacing is explained as follows. The coatings which possess lower particle-particle spacing, have more homogeneously dispersed WC particles (compare Fig. 16 (a) and 16 (c)). The WC reinforcing particles restrict the path of cracks developed under external loading and act as crack arrestors or crack deflectors [9, 32, 40]. With an increase in the content of WC wt.% in the coating and decrease of particle-particle spacing, a greater number of particles participate in crack deflection and hence limiting the plastic deformation of the metal matrix. In addition to acting as crack deflectors and crack arrestors, a decrease in mean free path further suppress the ability of the coalescence of any nucleated voids that grow under external loading. This inability of the voids to coalescence restrains the propagation of cracks in the MMC, and hence increasing the strain to failure. In a displacement controlled tensile testing, an increase in strain to failure would ultimately result in the increased tensile strength as the specimen would fail at higher external load.

3.6 Effect of average particle size on mechanical properties

The size of the reinforcing particles in the metal matrix affect the mechanical properties of the MMC [9, 36, 71–73]. In cold spray deposition of powder, due to the impact of the powder

particles with the substrate and previously deposited layers, the powder particles disintegrate and a reduction in particle size is observed [12, 28]. The reduction in the size of incoming particles is higher for the powders consisting of the higher content of WC wt.% [28]. This is because in the powder with a higher content of WC wt.%, a greater number of particles impinge the substrate and hence more fragmentation of the particles.

This thesis investigates the effect of particle size (ϕ) on the tensile strength of the cold sprayed WC-Ni MMC coatings. Given the irregular shape of the reinforcing WC particles (see Fig. 21), the size of the particles was estimated by measuring the average area of the particles [76]. Table 3 indicates that with an increase in the content of WC wt.% in the coating, there is an increase in the tensile strength of the coating. Further, Table 4 suggests that with an increase in the content of WC wt.% in the coating, there is a reduction in the average particle size of the WC in the coating. For example, for a coating containing 6.35 ± 0.06 wt.% WC, the average particle size is 19.37 ± 0.44 μm^2, compared to the average particle size of 7.24 ± 0.31 μm^2 at 34.92 ± 0.03 wt.% WC in the coating.

Relationships such as the Hall-Petch and Griffith criteria for fracture [77], where particle size is related to the strengthening of the metals persuaded hypothesis in this examination toward a comparable connection between the tensile strength and the particle size of the WC in the cold sprayed coatings, which is given as,

$$\sigma \propto \frac{1}{\sqrt{\phi}}. \tag{25}$$

For the cold sprayed WC-Ni coatings tested in this study, the tensile strength as a function of $\frac{1}{\sqrt{\phi}}$ is shown in Fig. 22. Figure 22 indicates great concurrence with the proposed structure as it demonstrates an almost straight connection between the tensile strength of the as-sprayed MMC coatings and $\frac{1}{\sqrt{\phi}}$. An increase in tensile strength with a decrease in average particle size is explained as follows.

The smaller average reinforcing particle size permit for lower particle-particle mean free path and hence strengthening of MMC as detailed in the previous section. Moreover, smaller average reinforcing particle size supplements the strengthening of the matrix due to an increase in the number of dislocations at the particle-matrix interface [64, 71]. The dislocations strain hardens the MMC and increases the failure strength [24]. The dislocations are generated under thermal and mechanical properties mismatch at the particle-matrix interface [24]. In the fabrication of the cold sprayed MMC, this mismatch in properties is further enhanced due to high velocity and temperature gradient existing in the fabrication process. In totality, a higher WC wt.% and smaller average particle size, results in more interfacial area between the particle and the matrix (as explained in section 4.3). This increase in the interfacial area potentially increases the development of dislocation sites. Kouzeli, *et al.* [64] also investigated the concept of strengthening of the MMCs due to an increase in the number of dislocations. They distinguish the dislocations as geometrically necessary dislocations (GNDs) and statistically stored dislocations (SSDs). GNDs are formed amid the external loading and are vital for the consistence deformation of the material. Conversely, SSDs generate by virtue of the manufacturing process.

An increase in the WC wt.% in the feedstock powder increase the number of SSDs. This is because the Ni metal gets work harden with a higher number of incoming particles impacting the substrate and the previously deposited powder layers. Additionally, in cold spray, an increase in WC wt.% in the feedstock powder is accompanied by a decrease in average particle size in the coating (see Table 4). This decrease in average particle size is likely to increase the potential sites for the generation of GNDs and hence the strengthening. Even though the quantification of the dislocations is difficult, they assume a critical part in the strengthening of the metal matrix [64].

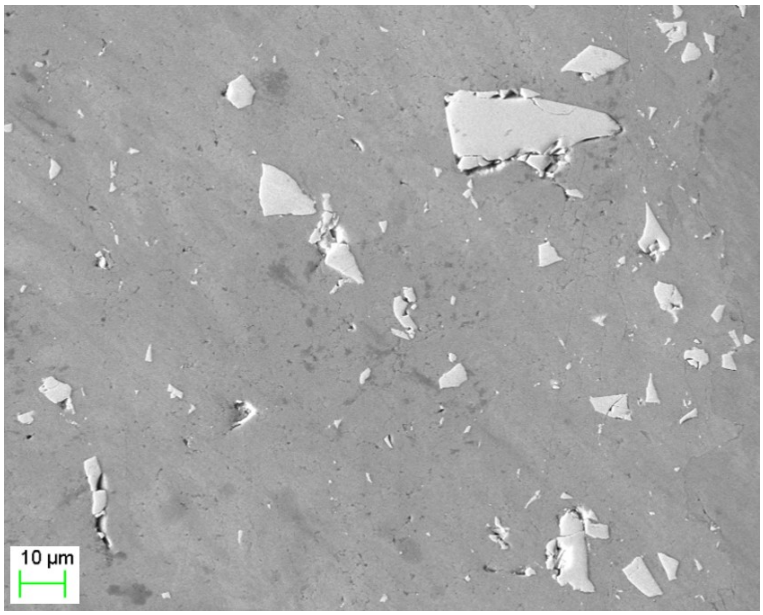

(*a*)

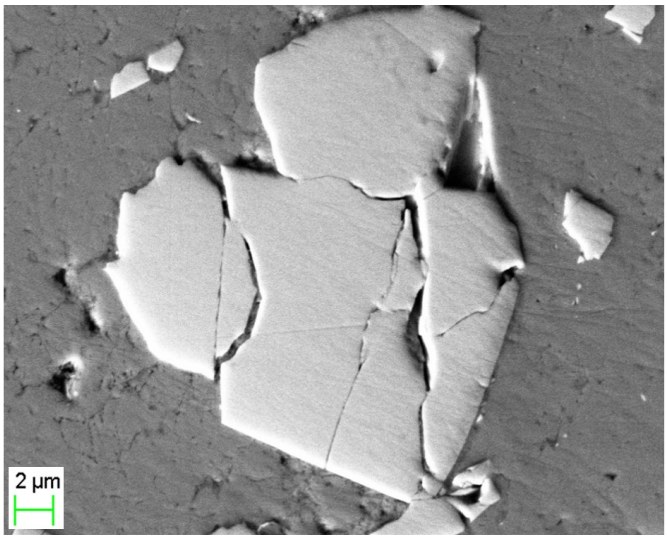

(*b*)

Figure 21: SEM micrographs indicating the irregular morphology of the deposited WC particles at magnification (*a*) ×500 and (*b*) ×2000.

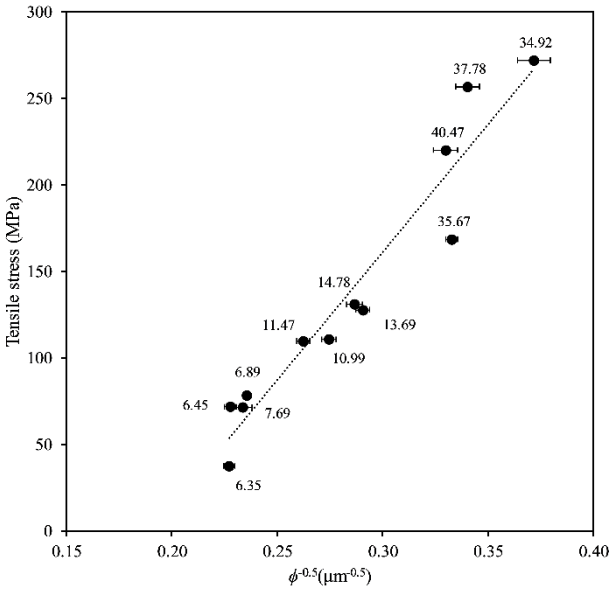

Figure 22: Tensile strength of cold sprayed MMC coatings versus the inverse square root of the average WC particle size in the coating. The wt.% of the WC particles in the coating is indicated on the plot.

3.7 Effect of porosity on mechanical properties

The porosity (θ) in the cold sprayed MMC coatings affects their mechanical properties [12, 15, 28]. Table 4 suggests that with an increase in the carbide content of the coating, the porosity of the coatings decreases. For example, porosity of 0.48 ± 0.03 vol.% at 6.35 ± 0.06 wt.% WC, decreased to 0.037 ± 0.004 vol.% at 34.92 ± 0.03 wt.% WC in the coating (see Table 4). Also, Table 3 and Table 4 suggests that with a decrease in porosity of the coating, the tensile strength of the coatings increased. For example, the tensile strength of 37.91 MPa at 6.35 ± 0.06 wt.% WC increased to 276.09 MPa at 34.92 ± 0.03 wt.% WC in the coating. Therefore, in addition to the particle size, particle-particle mean free path, and the particle-matrix interfacial area, the increase in the tensile strength of the coating may also be linked to the decrease in the porosity of the coating. A decrease in porosity at higher wt.% of WC in the coatings is due to better consolidation of Ni metal matrix at higher wt.% of WC. This is because, at higher wt.% of WC, a greater number of particles impinge the substrate and previously deposited layers and hence solidifying the metal matrix [15, 24, 26, 28]. This consolidation of the metal matrix at higher wt.% of WC subsequently provides enhanced ability to transfer the external load from the metal matrix to the stiffer carbide [28]. The Fig. 23 shows the plot of tensile strength as the function of the inverse of porosity of the coating. It shows that with a decrease in porosity of the coating, the tensile strength increases. This may be represented in equation form as,

$$\sigma \propto \frac{1}{\theta}. \tag{26}$$

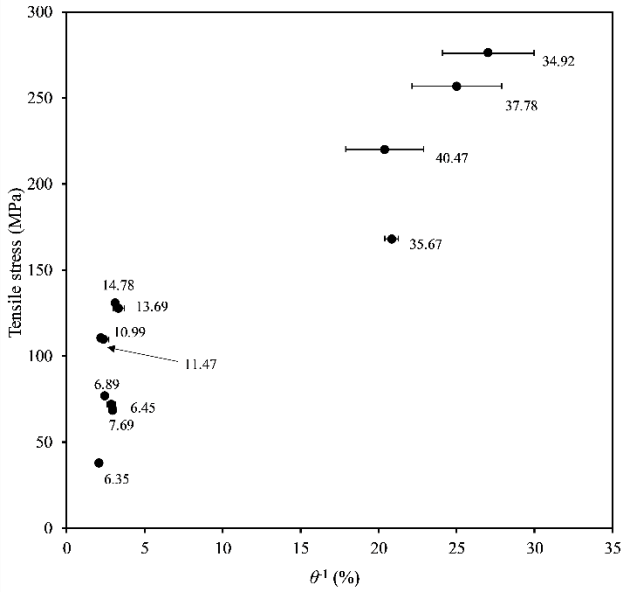

Figure 23*:* Tensile strength of cold sprayed MMC coatings versus the inverse of porosity in the coating. The wt.% of the WC particles in the coating is indicated on the plot.

3.8 Relationship between microstructure and mechanical properties of the cold sprayed tungsten carbide-nickel MMC coatings

The previous sections detail the effect of the microstructural feature on the tensile strength of the coatings when studied independently. However, it is often that the microstructural features like the reinforcing particle content, the average particle size, particle-particle mean free path, and porosity are inter-dependent. For example, a decrease in the average particle size of the reinforcing particles permits the particles to come closer to each other and hence indirectly affect the particle-particle mean free path. Also, it is well documented for the cold sprayed coatings that with an increase in hard particle content in the coating, the porosity decreases [15, 28]. Therefore, it was deemed more appropriate that after identifying the functional relationship of the effect of individual microstructure on the tensile strength; it is plausible to study the

combined effect of studied microstructure on the tensile strength of the coatings. This is presented in Eq. (27), which is obtained by combining the Eqs. (23) to (26).

$$\sigma \propto \frac{\psi}{\sqrt{\phi} \times \sqrt{\lambda} \times \theta}. \tag{27}$$

The Fig. 24 shows the tensile strength as the function of independent variables presented in Eq. (27). This functional relationship, as appeared in Fig. 24 (a), proposes that there were two different tensile strength regimes, which were recognized when the content of reinforcing WC was less than 15 wt.% and when the content of reinforcing WC was beyond 30 wt.%. Interestingly, both the regimes showed a nearly linear relationship of tensile strength with the independent variables defined in Eq. (27). The linear relationship was confirmed by calculating the *R*-squared value for both the regimes. The Fig 24 (b), which represents the regime governed by the content of WC less than 15 wt.% had an *R*-squared value of 0.86 compared to 0.94 for the regime governed by the content of WC more than 30 wt.%. This difference in the tensile strength of the coating also manifested in the toughness of the coatings. The coatings with WC content less than 15 wt.%, the average energy absorbed to failure was approximately 0.04 ± 0.02 N/mm^2 (n = 8). Conversely, the coatings with WC content beyond 30 wt.%, the average energy absorbed to failure was approximately 0.13 ± 0.06 N/mm^2 (n = 4). This significant increase in the tensile strength of the coatings with WC beyond 30 wt.% may be partially explained by the exceptional decrease in the porosity of the coating beyond 30 wt.% of WC (see Table 4). It is likely that for the coatings consisting of WC less than 15 wt.%, the collapsing of the higher number pores under external loading may induce higher damage accumulation and ultimately the failure of the coatings. This is detailed in the next section.

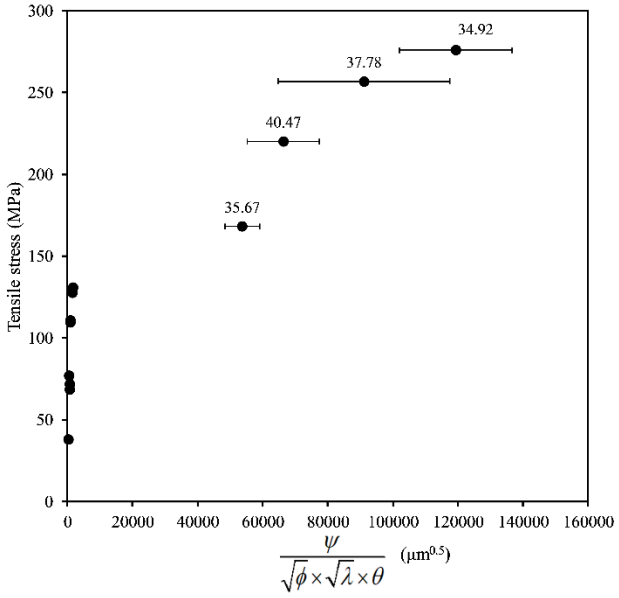
Tensile stress (MPa)
300
250
200
150
100
50
0
0
20000
40000
60000
80000
100000
120000
140000
160000
34.92
37.78
40.47
35.67
$\frac{\psi}{\sqrt{\phi}\times\sqrt{\lambda}\times\theta}$ (μm$^{0.5}$)

(*a*)

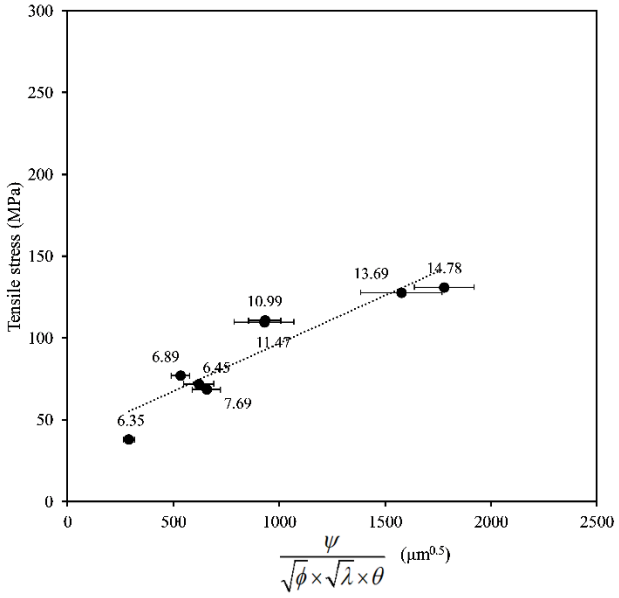
Tensile stress (MPa)
300
250
200
150
100
50
0
0
500
1000
1500
2000
2500
13.69
14.78
10.99
11.47
6.89
6.45
7.69
6.35
$\frac{\psi}{\sqrt{\phi}\times\sqrt{\lambda}\times\theta}$ (μm$^{0.5}$)

(*b*)

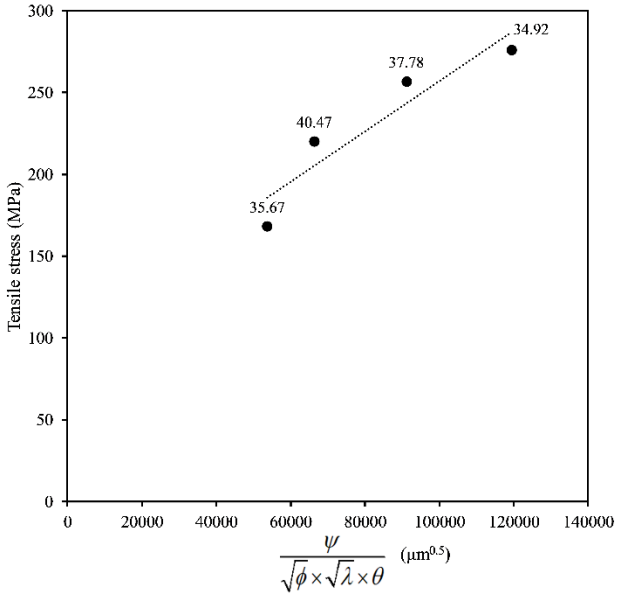

(*c*)

Figure 24: Tensile strength of cold sprayed MMC coatings versus the independent variable of particle-matrix interfacial area, particle-particle mean free path, average WC particle size, and coating porosity with (*a*) WC content less than 15 wt.% and more than 30 wt.%, (*b*) WC content less than 15 wt.%, and (*c*) WC content more than 30 wt.%. The wt.% of the WC in the coating is indicated on the plot.

3.9 Failure of MMC coatings

The initial damage accumulation in the fabricated coatings was studied and analyzed by plotting the axial strains versus the lateral strains for the conducted tensile tests (see Fig. 25). The extraction of the lateral strains was made feasible by the DIC technique, which was otherwise difficult to calculate by using the extensometers. In tensile testing, the axial extension of the dogbones causes lateral movement of the material. This lateral displacement plays a vital role in

the overall damage of the material and its failure. Therefore, the study of lateral strains as a function of axial strains becomes essential. The curves in Fig. 25 suggest that the lateral strains are a complex function of the axial strain near the failure strain of the coatings. The failure strain is accompanied by a dramatic change in the slope of the curves (see Fig. 25 (a)). Here, the curve corresponding of 0.45 ± 0.11 porosity was omitted because of a high variability in the lateral strain data near the failure strains. The lateral strain was deemed outlier as the curve showed two inflection points in the vicinity of the failure strains. This was irrational and accounted to the poor speckle resolution due to the large displacements in the subsets near the failure of the specimen. However, the curve was considered while calculating the slope of the curves as shown in Fig. 25 (b).

The slope of the curves in Fig. 25, which is equivalent of Poisson's ratio was quantified to study the effect of initial damage on the tensile strength of the coatings. The slopes of the curves were measured at approximately 0.006 % axial strain. The Fig. 25 (b), which presents the enlarged view of the strain data at the onset of the tensile experiment, was employed to calculate the Poisson's ratio. The magnitude of the average of Poisson's ratio for the coatings with higher porosity and content of WC less than 15 wt.% (solid curves) was approximately 0.41 ± 0.24 (n = 8). In contrast, the magnitude of the average of Poisson's ratio for the coatings with lower porosity and content of WC more than 30 wt.% was approximately 0.23 ± 0.06 (n = 4). The average Poisson's ratio of 0.23 ± 0.06 (n = 4) for the coatings with the content of WC more than 30 wt.% is comparable to the bulk Poisson's ratio of Ni, which is approximately 0.31 [17]. A higher average slope for the coatings with higher porosity and content of WC less than 15 wt.% suggests that that the material may be drifting laterally inwards to fill the pores of the coating.

This lateral displacement may induce high initial damage in the coatings and hence, lower strength [78]. For example, for a coating with higher porosity of 0.48 ± 0.14 vol.% and 6.35 ± 0.06 wt.% WC, the magnitude of Poisson's ratio is approximately 0.95 and the tensile strength is 38 MPa. In comparison, a coating with lower porosity of 0.042 ± 0.023 vol.% and higher content of WC of 37.78 ± 0.04 wt.%, the magnitude of Poisson's ratio is approximately 0.15 and hence the higher tensile strength of 257 MPa. An enlarged view of the slopes is shown as an aid to readers in Fig. 25 (b). The comparison of the average of Poisson's ratio of the two discussed regimes confirms that indeed, porosity determines the damage and failure in the coatings. However, Fig. 25 (b) also shows variability with the explanation of damage accumulation and failure solely based on porosity. For example, a coating with 0.35 ± 0.12 vol.% porosity and 6.45 ± 0.11 wt.% WC, the magnitude of Poisson's ratio is 0.18, compared to the higher magnitude of Poisson's ratio of 0.33 at 0.049 ± 0.01 vol.% porosity and 40.47 ± 0.03 wt.% WC (see Fig. 25 (b)). Thus, as suggested by Fig. 25 (b), there is higher damage accumulation for coating with lower porosity and higher WC wt.% and it should be followed by a lower tensile strength. However, the tensile strength of 40.47 ± 0.03 wt.% WC coating is higher, than the coating with 6.45 ± 0.11 wt.% WC in the coating (see Fig. 18 and Table 3). Therefore, it would be imprudent to generalize the trend of damage accumulation and failure of cold-sprayed WC-Ni MMC coatings based on the data of vol.% of porosity. This was also observed by Holmberg, *et al.* [32] and they noted that in addition to porosity, the localized effect of other microstructural features like particle morphology, mean free path, particle size, and defects also immensely influence the mechanical properties of the coatings and their effect may not be ignored. Moreover, they considered defects to be the critical determining factor affecting the mechanical and wear properties of the thermal sprayed coatings [32, 33]. Figure 25 provides another evidence that

though the damage in the coatings may be related to the vol.% of porosity, yet the failure of coatings is a broader phenomenon, affected by the concert of microstructural features and manufacturing defects [78, 79]. This enhances the importance of studying the combined effect of microstructure, as explained by Eq. 27. Further investigation is required; however, Eq. 27 may provide preliminary understanding to elicit the relationships between microstructure and tensile strength of WC-Ni MMC coatings as a function of the different microstructural features of the coating.

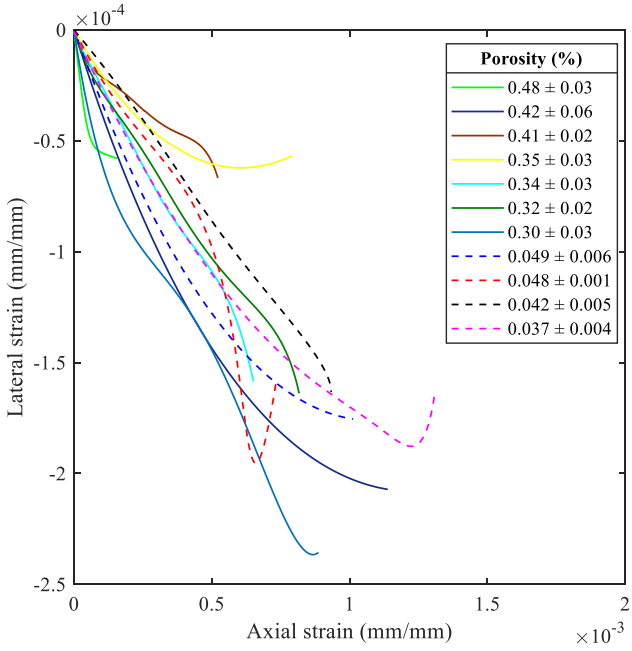

(*a*)

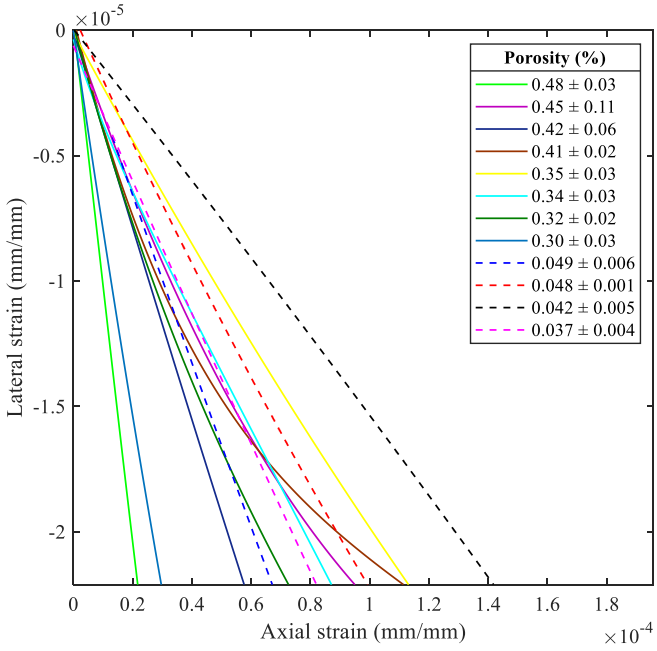

(*b*)

Figure 25 Axial strains versus the lateral strains for the fabricated cold sprayed WC-Ni MMC coatings. (*a*) Plot showing the curves for full duration of tensile testing and (*b*) Plot showing the strains for the initial segment of the loading.

3.10 Preliminary modelling of mechanical response

This section presents the definition and the results of a preliminary model that was used to predict the tensile stress-strain behaviour of the cold sprayed WC-Ni MMC coatings. The definition of the micro-mechanism model is based on the material models that were available in the commercial software, Digimat-FE [80]. Upon validation of the model with the experimental results, the model was further employed to predict the effect of particle-matrix interfacial strength on the tensile strength of the studied RVE.

Based on the literature and the material models available in Digimat-FE, it was assumed that the mechanical behaviour of Ni metal matrix in the MMC to be elasto-plastic with J_2 plasticity model [80–82]. The J_2 plasticity model is based on the von Mises equivalent stress, σ_{eq} [80], defined as,

$$\sigma_{eq}^2 = J_2(\sigma) = \frac{1}{2}\left[\left(\sigma_{11}-\sigma_{22}\right)^2 + \left(\sigma_{22}-\sigma_{33}\right)^2 + \left(\sigma_{33}-\sigma_{11}\right)^2\right] + \left[\sigma_{12}^2 + \sigma_{23}^2 + \sigma_{31}^2\right]. \quad (28)$$

The von Mises equivalent stress reduces to simple tensile stress for the uniaxial loadings. Thus, it was assumed that the tensile stress-strain relation of Ni follows the power law of hardening given as [71],

$$\sigma = A\varepsilon^n, \quad (29)$$

where the symbols σ, A, and n are the axial stress, the hardening modulus, and the hardening exponent. The mechanical behaviour of WC was assumed to be isotropic elastic [71, 81]. As discussed in the introduction of this thesis, the failure of the MMC at the particle-matrix interface is prominent in MMCs and is one of the defining factors in the failure of the material [50, 60, 71]. Thus, to incorporate the effect of the particle-matrix interface in the model, defining a cohesive zone was crucial. The cohesive zone models the surrounding environment of the reinforcing particle and is used to model the debonding at the interface [71, 80]. The developed model defines a cohesive region around the reinforcing particles, as shown in Fig. 26 with a thickness of 0.0028 mm. The initiation of damage of the cohesive zone was based on the maximum stress criterion, defined as,

$$\max\left\{\frac{\langle t_n \rangle}{t_n^0}, \frac{t_s}{t_s^0}, \frac{t_t}{t_t^0}\right\} = 1, \quad (30)$$

where symbols t_n, t_s and t_t, are respectively the tensile strength in the normal mode and shear only mode (first and second shear direction) [80] and the corresponding denominators in Eq. (30) represent their maximum value. In Digimat-FE, the values that need to be defined are for the denominators in Eq. (30). Using the trial and error method, the final material properties that were used for the Ni matrix and WC particles to validate the experimental curve are summarized in Table 5.

The microstructure of the RVE was defined in the Digimat-FE. The RVE consists of the average particle size as calculated from the SEM images of the fabricated coatings (see Fig. 16b). In this study, the shape of particles is assumed to be ellipsoid with an aspect ratio equal to one. In the future, particle shapes may be varied. The geometry of the microstructure is shown in Fig. 26. There are 29 ellipsoid particles generated with an average particle size of 12.2 μm (see Fig. 26). This RVE was meshed using the C3D10M elements with the software suggested minimum element size. The RVE was quasi-statically loaded with displacement-controlled setup up to the failure. A similar displacement-controlled boundary conditions were employed by Su, *et al.* [71] to model the tensile behaviour of the silicon carbide reinforced aluminium MMC. The developed framework was then numerically solved using the finite element solver provided by the Digimat-FE. The obtained stress-strain curves were compared with the experimental results and using the trial and error method, the resultant stress-strain curves from the Digimat-FE were approximately matched with the experimental stress-strain curve by tuning the Young's modulus and the tensile strength properties of the Ni material. The Young's modulus of Ni is approximately 207 GPa [17]; however, a Young's modulus of 150 GPa was used to validate the experimental curve. Similarly, Nan, *et al.* [57] reported the cohesive strength to vary as the inverse square root of the

particle size in the matrix. However, a lower cohesive failure strength was used than predicted from the relationship from Nan, *et al.* [57] (see Fig. 27). A lower value of both Young's modulus and the tensile strength of Ni used to validate the numerical curve may be related to the evolution of damage in the tested coatings under tensile loading and is explained in the next section.

Table 5: Mechanical properties of the matrix and the particle used to validate the model.

Property	**Matrix (Ni)**	**Particle (WC)**
Density	8,900 kg/m^3 [26]	15,800 kg/m^3 [26]
Young's modulus	150 GPa [experimental]	675 GPa [83]
Poisson's ratio	0.31 [17]	0.24 [83]
Yield stress	163 [17]	-
Hardening modulus	648 [17]	-
Hardening exponent	0.33 [17]	-

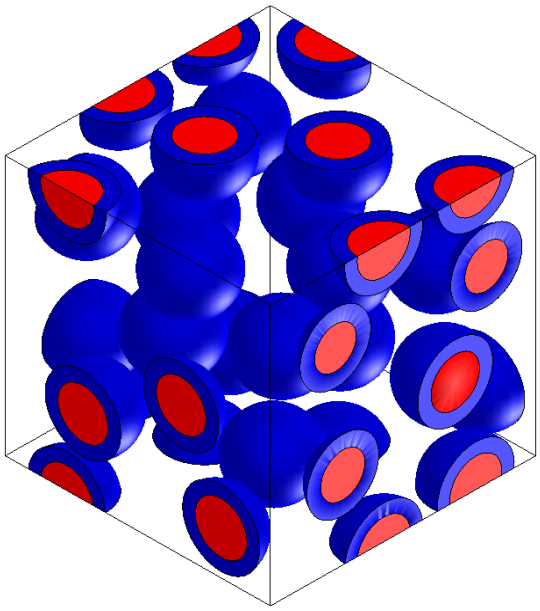

Figure 26: RVE of the microstructure. Red color represents the hard-reinforcing particles and the blue color represents the cohesive zone.

Upon validation of the model, the effect of interfacial strength was studied using the developed model. Keeping all the defined material properties, microstructure, and loadings constant, the failure strength of the cohesive elements, defined by the continuum metal matrix material (here, Ni) was changed. The different curves obtained from changing the interfacial strength are presented in Fig. 27. Fig. 27 presents the curves for the microstructure with approximately 14.78 ± 0.04 wt.% WC in the coating and the average particle size of 12.2 μm. It was observed that the initial part of the stress-strain curve is matched to a good approximation with the experimental curve (see blue curve in Fig. 27). However, as the axial strain progresses, both the experimental and numerical curve start deviating from each other. The experimental curves exhibit an onset of damage at a lower strain than the numerical model. For example, at approximately 0.05% strain, the experimental curve starts deviating from the validated

experimental stress-strain curve. This deviation may be attributed to the fact that as explained in section 4.8 of this thesis, the damage and the failure is a highly complex phenomenon and may not be defined adequately by Eq. (30). As observed from the shape of the curves in Fig. 25a, the lateral strains are a complicated function of the axial strains, indicating that the damage evolution function needs to microstructurally informed and may not be defined based on the maximum stress criteria. This reiterates to the importance of models which incorporates the microvoid nucleation and growth as described in the Chapter 2 of this thesis [55]. Amirian, *et al.* [81, 82] have shown that for ceramic-metal composites, the damage may be simulated using the Gurson model which is a microstructure (particle shape, size, and aspect ratio) equipped model to predict the stress-strain response. Further, the debonding in the tested coatings is a complex function of stress at the interface, a function of porosity, particle size, mean free path, and defects in the coating [50, 51], which were ignored in defining the model. Moreover, in the derivation of the numerical model, it was assumed that the shape of the particles is ellipsoid; however, the actual shape in the tested coating is irregular (see Fig. 21). All these factors contribute towards the deviation of the experimental and numerical curves; however, this model may advise the first approximations of the interfacial strength values for the low-pressure cold sprayed coatings. The observed value for the validated curve was approximately 215 MPa. Nan, *et al.* [57] reported the cohesive interfacial strength to be proportional to the inverse of the square root of particle size. Thus, based on this criterion, the cohesive interface strength for the average particle size of 12.2 μm would be 286 MPa. A lower value in the present model is may be either due to the simplification of the model or may be the characteristic of the cold sprayed coatings. Overall, this needs to be further explored using other numerical models which incorporate the spectrum of microstructural properties.

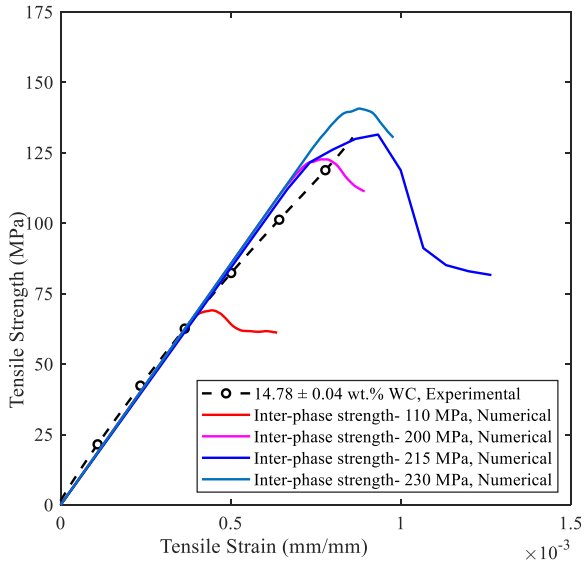

Figure 27: Experimental and modelled tensile stress strain curves for 14.78 ± 0.04 wt.% WC in the coating. The inter-phase strength used in the numerical models is marked on the plot.

4 Conclusions

In this thesis, three different feedstock powder blends were prepared to be deposited by the low-pressure cold spray process. The powders were varied based on the content of WC wt.% in the powder blend. The powders consisted of 50 wt.% WC + 50 wt.% Ni powder blend, 71 wt.% WC + 29 wt.% Ni powder blend, and 92 wt.% WC + 8 wt.% Ni powder blend. The fabricated coatings were utilized to prepare the tensile dogbone coupons to study their mechanical properties, namely the tensile strength, the Young's modulus, and the toughness. Through tensile testing, it was found that an increase in the carbide content in the coating from approximately 6.35 ± 0.06 wt.% WC in coating to 34.92 ± 0.03 wt.% WC in coating there was:

- Increase in failure stress from 37.91 MPa to 276.09 MPa;
- Increase in strain to failure from 0.036% to 0.14%;
- Increase in Young's modulus from 121 GPa to 233 GPa; and
- Increase in toughness from 0.006 N/mm^2 to 0.199 N/mm^2.

This improvement in the mechanical properties was explained and credited to the refined microstructural features of the coatings, which included:

- Increase in the particle-matrix interfacial area from approximately 5586 ± 147 μm^2 at 6.35 ± 0.06 wt.% WC to 42834 ± 3960 μm^2 at 34.92 ± 0.03 wt.% WC due to increase in the number of reinforcing WC particles in the fabricated MMC.

- Reduction in porosity of coating from approximately 0.48 ± 0.03 % at 6.35 ± 0.06 wt.% WC to 0.037 ± 0.004 % at 34.92 ± 0.03 wt.% WC in the coating due to better consolidation of matrix at higher carbide content in cold spray;
- Reduction in average particle size of the reinforcing particles from approximately 19.37 ± 0.44 μm at 6.35 ± 0.06 wt.% WC to 7.24 ± 0.31 μm at 34.92 ± 0.03 wt.% WC in the coating due to in-flight carbide particle interaction and fracturing of carbides upon impact to the surface of the substrate and previously deposited metal matrix; and
- Reduction in particle-particle mean free path from approximately 83 ± 10 μm at 6.35 ± 0.06 wt.% WC to 13 ± 0.4 at μm at 34.92 ± 0.03 wt.% WC in the coating due to decrease in distance between carbide particles at higher carbide content.

In addition to the classical explanation of the increase in the mechanical properties with an increase in the content of reinforcing phase in the MMC; this study develops functional relationships between the microstructure and the tensile strength of the cold sprayed WC-Ni MMC coatings. A framework constituting of the combined microstructural effect on the tensile strength indicated different regimes of the tensile strength of the coating. The high strength regime which was governed by the content of WC beyond 30 wt.% in the coating was contrasted with the comparatively low strength regime, governed by the content of WC less than 15 wt.%. This claim of different strength of tensile strength regime was further strengthened by quantifying the toughness and the damage in the coatings. A significant increase in the average toughness and average Poisson's ratio was noted in the coatings with the content of WC beyond 30 wt.% compared to the coatings with the content of WC less than 15 wt.%. Lastly, this study concludes with a preliminary attempt to model the tensile stress-strain behaviour of coatings with

the incorporation of the cohesive zone modelling. The microstructure-average particle size informed model suggests that an increase in the interfacial strength is likely to increase the tensile strength of the coating. The onset of damage in the microstructure of the experimental stress-strain curve was observed to begin at a lower axial strain compared to the modelled stress-strain curve. This indicated that the incorporation of other microstructural features, such as porosity, particle-particle mean free path, and shape of the particle in the constitutive equation is necessary and may not be ignored. The major contributions from this thesis are presented below:

- To date, the literature had limited studies that explored the mechanical properties such as tensile strength, Young's modulus, and toughness for the low-pressure cold sprayed MMC coatings. Therefore, the thesis addresses this gap and documents the calculated values for the tensile strength, Young's modulus, toughness, and Poisson's ratio for the tested low-pressure cold sprayed WC-Ni MMC coatings.
- Recognizing that there is an approximate direct relationship between the tensile strength and interfacial area between the reinforcing particles and metal matrix.
- Recognizing and establishing that there is a linear relationship between the tensile strength and the square root of the inverse of the average particle size and mean free path between the reinforcing particles.
- Recognizing and establishing that there is an inverse relationship between the tensile strength and porosity of the coatings.
- Establishing a framework based on the functional relationship of the studied microstructure and tensile strength of the tested coatings. This study reports distinct regimes in the tensile

strength of the coatings based on the content of WC wt.% in the coatings. This claim is supported by the calculated average toughness and average Poisson's ratio values.

- This thesis layout the importance of DIC data by measuring the lateral strains, which otherwise would be impossible to quantify using the traditional extensometers. The lateral strain data was vital to calculate the Poisson's ratio and provide a damage-based explanation of the failure of the low-pressure cold sprayed coatings.

5 Future Work and Recommendations

To examine the influence of microstructure on mechanical properties, more laboratory experiments may be conducted; however, they are arduous and expensive to perform. These experimental studies limit the investigation to study the influence of single or combined microstructural features as it may not be feasible to independently control parameters like porosity, particle size, mean free path, interfacial area, and many other. These limitations and constraints on experimental testing of the MMC coatings warrant the need for modelling of the mechanical properties and behavior of the MMC coatings in order to understand the coatings better under various applied loading conditions [9, 41–44]. The data collected for the mechanical properties in addition to the microstructural features such as porosity, particle-particle mean free path, and the average size of the carbide particles may be incorporated in the mechanism-based Gurson model [54, 55, 81]. The importance of the microstructure-based model is presented in the introduction of this thesis. In the Gurson model, the matrix is assumed to exhibit elasto-plastic behavior and the particles are isotropic-elastic [55]. For the numerical analysis, the randomly distributed particle geometry may be generated in the Digimat-FE software and further may be solved numerically in the finite element software, ABAQUS. Thus, the numerical model may be utilized to predict the stress-strain response of the fabricated MMC coatings and validated with the performed experimental tensile test data. Further, upon validation of the Gurson model, finite element method based MMC modelling may be utilized to enhance the understanding of the sensitivity of mechanical response of a coating to microstructural changes without the obligation to conduct the physical experiments. Material models like kinematic hardening model may be employed for the metal matrix to model the cyclic loading [80]. Incorporation of models that

cater to cyclic loading is of importance because the erosive wear in the Oil & Gas industry constitutes of the continuous interaction of hard particles with the protective coating and thus, results in cyclic loading. Further, Llorca, *et al.* [84] noted that MMCs failure is not exclusively limited to the failure of metal matrix and/or particle-matrix debonding. Fracture of reinforcing particles is evident at high-stress loadings and therefore, a holistic numerical wear model needs to incorporate the fracture of the reinforcing particles as well. Initially, the incorporation of the fracture of the reinforcing particle may be explored by defining a crack initiation criterion for the reinforcing particles [80]. Criteria such as maximum principal tensile strength may be prescribed for the initiation of crack, similar to the metal matrix [80].

This work documents the novel results for the mechanical properties of the cold sprayed WC-Ni MMC coatings, which includes the Young's modulus, tensile strength, strain to failure, and the toughness. As discussed in the introduction, many researchers have noted the importance to study the full field testing of the coatings [62, 63, 65]; however, limited studies are available in the literature. This study addresses the literature gap for low-pressure cold sprayed WC-Ni coatings; however, there are other carbide-based cold sprayed coatings for which the full-field tested mechanical properties are not available in the literature. For example, Lee, *et al.* [28] noted that boron carbide-based low-pressure cold sprayed coating has a similar hardness and adhesion strength values as the tungsten carbide coatings. Also, Vackel, *et al.* [62] conducted tensile testing on the metal coatings that were fabricated using the thermal spray process; however, they loaded both the substrate and the coating together. Thus, they did not examine the mechanical properties of the as-sprayed coating material. A similar strategy as presented in this thesis to extract mechanical properties, such as Young's modulus, tensile strength, and the

toughness for the cold sprayed pure metals and other carbide-based materials may be employed. An investigation into the mechanical properties of the cold sprayed pure metals and contrasting it with the cold sprayed MMCs may strengthen the importance of the incorporation of the carbides into the metal matrix to enhance the performance metrics of the coatings.

This study offers a framework of diagnosis to investigate the effect of the particle-matrix interfacial area, particle-particle mean free path, average particle size, and porosity on the tensile strength of the cold sprayed WC-Ni coatings. This framework may be tested for its validity for the other carbide-based coatings and thermally sprayed coatings. This would advance the literature towards a general functional relationship to predict the tensile strength of the thermally sprayed coatings based on the observed microstructure in the coating.

References

[1] A. Al-Hamed, H.Y. Al-Fadhli, S. Al-Mutairi, B.S. Yilbas, M.S.J. Hashmi, J. Stokes, Investigation of HVOF thermal sprayed nanostructured WC-12Co mixed with Inconel-625 coatings for oil/gas applications, in: Surf. Eff. Contact Mech. XI, WIT Press, Southampton, 2013: pp. 215–225.

[2] R. Gonzalez, H. Ashrafizadeh, A. Lopera, P. Mertiny, A. McDonald, A Review of Thermal Spray Metallization of Polymer-Based Structures, J. Therm. Spray Technol. 25 (2016) 897–919.

[3] G. Fisher, T. Wolfe, Protective overlays and coatings used in oil sands, ASM Handbook 5A, "Thermal Spray Technology", Ed. R.C. Tucker, 2003.

[4] P.L. Fauchais, J.V.R. Heberlein, M.I. Boulos, Thermal Spray Fundamentals, Springer US, Boston, MA, 2014.

[5] I.A. Ibrahim, F.A. Mohamed, E.J. Lavernia, Particulate reinforced metal matrix composites - A review, J. Mater. Sci. 26 (1991) 1137–1156.

[6] N. Chawla, K.K. Chawla, Metal Matrix Composites, Springer New York, New York, NY, 2013.

[7] R.C. Tucker, A.I.H. Committee, A.S. for M.T.S. Division, Thermal Spray Technology, ASM International, 2013.

[8] K.-H. Zum Gahr, Microstructure and wear of materials, Elsevier, Amsterdam; New York, 1987.

[9] N. Chawla, K. K. Chawla, Microstructure-based modeling of the deformation behavior of particle reinforced metal matrix composites, J. Mater. Sci. 41 (2006) 913–925.

[10] M. J. Neale, M. G. Gee, Guide to wear problems and testing for industry, William Andrew Pub, Norwich, N.Y, 2001.

[11] I. M. Hutchings, Tribological properties of metal matrix composites, Mater. Sci. Technol. 10 (1994) 513–517.

[12] E. Irissou, J.G. Legoux, B. Arsenault, C. Moreau, Investigation of Al-Al 2 O 3 Cold Spray Coating Formation and Properties, J. Therm. Spray Technol. 16 (2007) 661–668.

[13] A. Moridi, S.M. Hassani-Gangaraj, M. Guagliano, M. Dao, Cold spray coating: review of material systems and future perspectives, Surf. Eng. 30 (2014) 369–395.

[14] P. Fauchais, G. Montavon, Thermal and cold spray: recent developments, Key Engineering Materials 384 (2008)1–59.

[15] Y.T.R. Lee, T. Hussain, G. Fisher, A. McDonald, Cold-Sprayed Metal Matrix Composites Coatings, in: Cold Spray Coatings – Recent Trends and Future Perspectives, Pasquale Cavaliere, Ed., Springer International Publishing AG, Switzerland, 2017. ISBN 978-3-319-67182-6

[16] A. Papyrin, Cold spray technology, Elsevier, Amsterdam; London, 2007.

[17] R. Ghelichi, S. Bagherifard, M. Guagliano, M. Verani, Numerical simulation of cold spray coating, Surf. Coat. Technol. 205 23-24 (2011) 5294–5301.

[18] T. Schmidt, F. Gärtner, H. Assadi, H. Kreye, Development of a generalized parameter window for cold spray deposition, Acta Mater. 54 (2006) 729–742.

[19] A. Sova, A. Papyrin, I. Smurov, Influence of Ceramic Powder Size on Process of Cermet Coating Formation by Cold Spray, J. Therm. Spray Technol. 18 (2009) 633–641.

[20] A. Sova, V.F. Kosarev, A. Papyrin, I. Smurov, Effect of Ceramic Particle Velocity on Cold Spray Deposition of Metal-Ceramic Coatings, J. Therm. Spray Technol. 20 (2011) 285–291.

[21] Q. Wang, K. Spencer, N. Birbilis, M.X. Zhang, The influence of ceramic particles on bond strength of cold spray composite coatings on AZ91 alloy substrate, Surf. Coat. Technol. 205 (2010) 50–56.

[22] H. Koivuluoto, P. Vuoristo, Effect of Powder Type and Composition on Structure and Mechanical Properties of Cu + Al_2O_3 Coatings Prepared by using Low-Pressure Cold Spray Process, J. Therm. Spray Technol. 19 (5) (2010) 1081–1092

[23] P. C. King, S. H. Zahiri, M. Z. Jahedi, Rare Earth/Metal Composite Formation by Cold Spray, J. Therm. Spray Technol. 17 (2) (2008) 221–227.

[24] K. J. Hodder, H. Izadi, A. G. McDonald, A.P. Gerlich, Fabrication of aluminum–alumina metal matrix composites via cold gas dynamic spraying at low pressure followed by friction stir processing, Mater. Sci. Eng. A 556 (2012) 114–121.

[25] N. M. Melendez, A. G. McDonald, Development of WC-based metal matrix composite coatings using low-pressure cold gas dynamic spraying, Surf. Coat. Technol. 214 (2013) 101–109.

[26] N. M. Melendez, V. V. Narulkar, G. A. Fisher, A. G. McDonald, Effect of reinforcing particles on the wear rate of low-pressure cold-sprayed WC-based MMC coatings, Wear 306 (2013) 185–195.

[27] Y. Xie, R. J. Llewellyn, D. Stiles, Amorphous diamond coating of tungsten carbide and titanium carbonitride for erosive slurry pump component service, Wear 250 (2001) 88–99.

[28] Y. T. R. Lee, H. Ashrafizadeh, G. Fisher, A. McDonald, Effect of type of reinforcing particles on the deposition efficiency and wear resistance of low-pressure cold-sprayed metal matrix composite coatings, Surf. Coat. Technol. 324 (2017) 190–200.

[29] ASTM, SG65-04 (2010) Standard Test Method for Measuring Abrasion Using the Dry Sand/Rubber Wheel Apparatus, ASTM International, West Conshohocken, PA, 2015 www.astm.org.

[30] ASTM, G99-05 (2016) Standard Test Method for Wear Testing with a Pin-on-Disk Apparatus, ASTM International, West Conshohocken, PA, 2015 www.astm.org.

[31] G. Y. Lee, C. K. H. Dharan, R.O. Ritchie, A physically-based abrasive wear model for composite materials, Wear 252 (3-4) (2002) 322–331.

[32] K. Holmberg, A. Laukkanen, E. Turunen, T. Laitinen, Wear resistance optimisation of composite coatings by computational microstructural modelling, Surf. Coat. Technol. 247 (2014) 1–13.

[33] K. Holmberg, A. Laukkanen, A. Ghabchi, M. Rombouts, E. Turunen, R. Waudby, T. Suhonen, K. Valtonen, E. Sarlin, Computational modelling based wear resistance analysis of thick composite coatings, Tribology International 72 (2014) 13–30.

[34] H. Qing, 2D micromechanical analysis of SiC/Al metal matrix composites under tensile, shear and combined tensile/shear loads, Materials & Design 51 (2013) 438–447.

[35] A. J. Gant, M.G. Gee, Wear of tungsten carbide–cobalt hard metals and hot isostatically pressed high speed steels under dry abrasive conditions, Wear 251 (2001) 908–915.

[36] A.A. Torrance, Modelling abrasive wear, Wear 258 (1-4) (2005) 281–293.

[37] W.M. Garrison, Khruschov's rule and the abrasive wear resistance of multiphase solids, Wear 82 (1982) 213–220.

[38] H. S. Kim, On the rule of mixtures for the hardness of particle reinforced composites, Mater. Sci. Eng. A. 289 (2000) 30–33.

[39] N. Axen, and S. Jacobson, A model for the abrasive wear resistance of multiphase materials, Wear 174 (1-2) (1994) 187–199.

[40] N. Chawla, V.V. Ganesh, B. Wunsch, Three-dimensional (3D) microstructure visualization and finite element modeling of the mechanical behavior of SiC particle reinforced aluminum composites, Scr. Mater. 51 (2004) 161–165.

[41] S. Houdkova, F. Zahalka, M. Kasparova, L.M. Berger, Comparative Study of Thermally Sprayed Coatings Under Different Types of Wear Conditions for Hard Chromium Replacement, Tribology Letters 43 (2011) 139–154.

[42] A. S. Shedbale, I. V. Singh, B. K. Mishra, Heterogeneous and homogenized models for predicting the indentation response of particle reinforced metal matrix composites, Int. J. Mech. Mater. Des. 13 (2017) 531–552.

[43] P. Kanouté, D.P. Boso, J. L. Chaboche, B. A. Schrefler, Multiscale Methods for Composites: A Review, Arch. Comput. Methods Eng. 16 (2009) 31–75.

[44] G. Bolzon, E. J. Chiarullo, P. Egizabal, C. Estournes, Constitutive modelling and mechanical characterization of aluminium based metal matrix composites produced by spark plasma sintering, Mechanics of Materials 42 (2010) 548–558.

[45] J. Huang, G. Wu, W. Sha, Finite Element Modeling of Properties Influence of Particle Characteristics in Particle Reinforced Metal Matrix Composite, Composites and Nanocomposites (2013) 1–20.

[46] J. Zhang, Q. Ouyang, Q. Guo, Z. Li, G. Fan, Y. Su, L. Jiang, E. J. Lavernia, J. M. Schoenung, D. Zhang, 3D Microstructure-based finite element modeling of deformation and fracture of SiCp/Al composites, Composites Science and Technology 123 (2016) 1–9.

[47] T. Sadowski, B. Pankowski, Numerical modelling of two-phase ceramic composite response under uniaxial loading, Composite Structures 143 (2016) 388–394.

[48] A. Abedini, Z.T. Chen, A micromechanical model of particle-reinforced metal matrix composites considering particle size and damage, Computational Materials Science 85 (2014) 200–205.

[49] K. Danas, N. Aravas, Numerical modeling of elasto-plastic porous materials with void shape effects at finite deformations, Composites: Part B: Engineering 43 (2012) 2544–2559.

[50] A. Needleman, S. Nutt, S. Suresh, V. Tvergaard, Matrix, reinforcement, and interfacial failure. In Fundamentals of Metal Matrix Composites, S. Suresh, A. Mortensen, and A. Needleman, eds., Butterworth-Heinemann, Boston, Ch. 13 (1993) 233–250.

[51] G. Bae, Y. Xiong, S. Kumar, K. Kang, C. Lee, General aspects of interface bonding in kinetic sprayed coatings, Acta Mater. 56 17 (2008) 4858–4868.

[52] J. Eshelby, The determination of the elastic field of an ellipsoidal inclusion and related problems, Proceedings of the Royal Society of London (1957) 376–396.

[53] T. Mori, K. Tanaka, Average stress in the matrix and average elastic energy of materials with misfitting inclusions, Acta Metall. Mater. 21 (1973) 571–574.

[54] A. L. Gurson, Continuum theory of ductile rupture by void nucleation and growth: Part I: Yield criteria and flow rules for porous ductile media, J. Eng. Mater. Technol 99 (1977) 2–15.

[55] Z.L. Zhang, C. Thaulow, J. édegard, A complete Gurson model approach for ductile fracture, Engineering Fracture Mechanics 67 (2000) 155–168.

[56] T. S. Cao, M. Mazière, K. Danas, J. Besson, A model for ductile damage prediction at low stress triaxialities incorporating void shape change and void rotation, International Journal of Solids and Structures 63 (2015) 240–263.

[57] C. W. Nan, D. R. Clarke, The influence of particle size and particle fracture on the elastic/plastic deformation of metal matrix composites, Acta Mater. 44 9 (1996) 3801–3811.

[58] A. Needleman, A continuum model for void nucleation by inclusion debonding, J. Appl. Mech. 54 (1987) 525–531.

[59] V. Tvergaard, Effect of fiber debonding in a whisker-reinforced metal, Mater. Sci. Eng. A 125 (1990) 203–213.

[60] N. Chandra, H. Li, C. Shet, H. Ghonem, Some issues in the application of cohesive zone models for metal–ceramic interfaces, Int. J. Solid. Struct. 39 (2002) 2827–2855.

[61] L. Fang, W. Liu, D. Du, X. Zhang, Q. Xue, Predicting three-body abrasive wear using Monte Carlo methods, Wear 256 (2004) 685–694.

[62] A. Vackel, T. Nakamura, S. Sampath, Mechanical Behavior of Spray-Coated Metallic Laminates, J. Therm. Spray Technol. 25 5 (2016) 1009–1019.

[63] G. M. Smith, S. Sampath, Sustainability of Metal Structures via Spray-Clad Remanufacturing JOM 70 4 (2018) 512–520.

[64] M. Kouzeli, A. Mortensen, Size dependent strengthening in particle reinforced aluminium, Acta Mater. 50 (2002) 39–51. A. K. Basak, A. Pramanik, C. Prakash, Mater. Sci. Eng. A 763 (2019) 138141.

[65] G. M. Smith, O. Higgins, S. Sampath, In-situ observation of strain and cracking in coated laminates by digital image correlation, Surf. Coat. Technol. 328 (2017) 211–218.

[66] Schreier, Hubert, Jean-José Orteu, and Michael A. Sutton. Image correlation for shape, motion and deformation measurements: Basic concepts, theory and applications. Vol. 1. Boston, MA: Springer-Verlag US, 2009.

[67] Vic-2D, Correlated Solutions Inc., Irmo, South Carolina. URL ⟨http:// correlatedsolutions.com/vic-2d/⟩.

[68] B. Pan, K.Qian, H. Xie, A. Asundi, Two-dimensional digital image correlation for in-plane displacement and strain measurement: a review, Meas. Sci. Technol. 20 (2009) 062001.

[69] ASTM E8/E8M-13a, Standard Test Methods for Tension Testing of Metallic Materials, ASTM International, West Conshohocken, PA, 2013. www.astm.org.

[70] D. L. McDanels, Analysis of stress-strain, fracture and ductility behaviour of aluminium matrix composites containing discontinuous SiC reinforcement, Metall. Trans. A 16A (1985) 1105–1115.

[71] Y. Su, Q. Ouyang, W. Zhang, Z. Li, Q. Guo, G. Fan, D. Zhang, Composite structure modeling and mechanical behavior of particle reinforced metal matrix composites, Mater. Sci. Eng. A 597 (2014) 359–369.

[72] D. J. Lloyd, Particle reinforced aluminium and magnesium matrix composites, International Materials Reviews 39 1 (1994) 1–23.

[73] S. H. Leigh, C. K. Lin, C. C. Berndt, Elastic response of thermal spray deposits under indentation tests, J. Am. Ceram. Soc. 80 (1997) 2093–2099.

[74] T. Gustafson, P. Panda, G. Song, and R. Raj, Influence of Microstructural Scale on Plastic Flow Behavior of Metal Matrix Composites, *Acta Mater.* 45 (1997) 1633–1643.

[75] I. Lee, C. Hsu, C. Chen, N. Ho, and P. Kao, Particle-Reinforced Aluminum Matrix Composites Produced from Powder Mixtures Via Friction Stir Processing, *Compos. Sci. Technol.* 71 (2011) 693–698.

[76] G. M. Nelson, J. A. Nychka, A. G. McDonald, Structure, phases, and mechanical response of Ti-alloy bioactive glass composite coatings, Mater. Sci. Eng. C 36 (2014) 261–276.

[77] A. A. Griffith, The phenomena of rupture and flow in solids, *Philosophical Transactions of the Royal Society of London A 221 (1921) 163–198.*

[78] J. D. Hogan, L. Farbaniec, T. Sano, M. Shaeffer, K.T. Ramesh, The effects of defects on the uniaxial compressive strength and failure of an advanced ceramic, Acta Mater. 102 (2016) 263–272.

[79] J. D. Hogan, L. Farbaniec, N. Daphalapurkar, K.T. Ramesh, On compressive brittle fragmentation, J. Am. Ceram. Soc. 99 (2016) 2159–2169.

[80] Digimat User's Manual, Release 2016.1 – Student Edition – June 2016.

[81] B. Amirian, H. Li, J. Hogan, An experimental and numerical study of novel nanograined (γ + α2)-TiAl/Al_2O_3 cermets, Mater. Sci. Eng. A. 744 (2019) 570–580.

[82] B. Amirian, H. Li, J. Hogan, The mechanical response of a α2(Ti3Al) + γ(TiAl) – nanograined Al_2O_3 cermet under dynamic compression: modeling and experiment, Submitted to Acta Mater. (2019).

[83] http://www.pacificparticulatematerials.com/tungsten-carbide-wc-powder/, accessed on 31 July 2019.

[84] J. Llorca, J. Ruiz, J. Healy, M. Elices, C. Beevers, Fatigue crack propagation in salt water, air and high vacuum in a spray-formed particulate-reinforced metal matrix composite, Mater. Sci. Eng. A. 185 (1994) 1–15.

Appendix A – MATLAB Code

```
clear;clc;
% Code used to plot the stress-strain curves. Provide a path to the excel
%file where data axial strain and tensile
% stress data is stored
filename= 'D1.xlsx';
% Use the xlsread function to read the axial strain and tensile stress
% values.
eyy= xlsread (filename,'E4:E5992');
TensileStress = xlsread (filename, 'D4:D5992');
% The data is smoothed using the sgolay filter.
A = sgolayfilt (eyy, 5,5987);
B = sgolayfilt (TensileStress, 5,5987);
% Plot the curve using the plot function.
plot (A, B,'-p','MarkerIndices',1:800:length(A),'LineWidth',1);
% Provide labels to the axis
xlabel ('DIC Tensile Strain (mm/mm)')
ylabel ('Tensile Stress (MPa)')
% Repeat this to plot all the tensile stress-strain curves.
```

Appendix B – SEM Images of Coating Microstructure

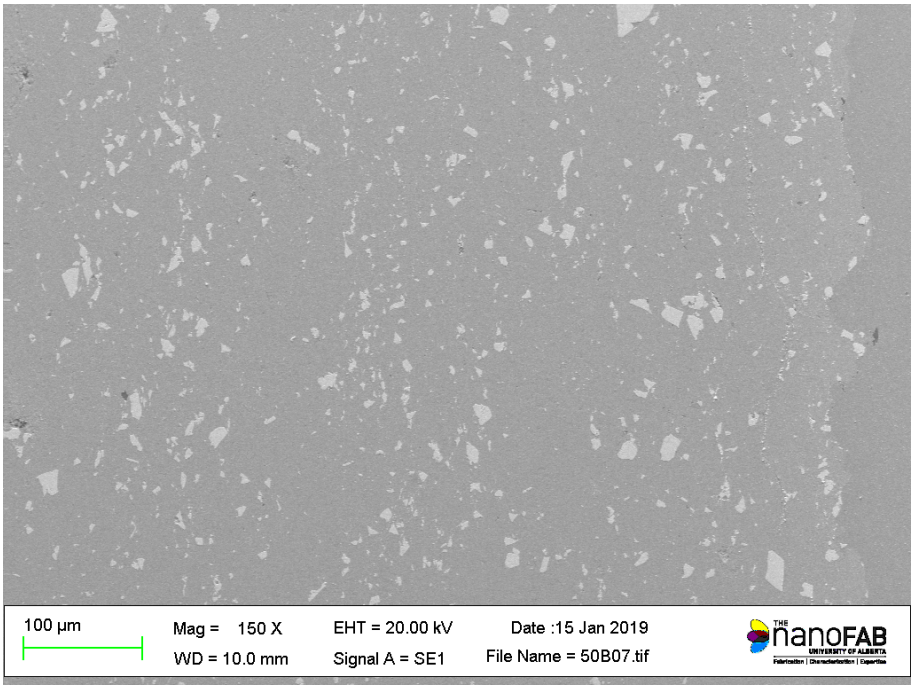

Figure B1: SEM image of the coating fabricated from the 50 wt.% WC + 50 wt.% Ni in the feedstock powder.

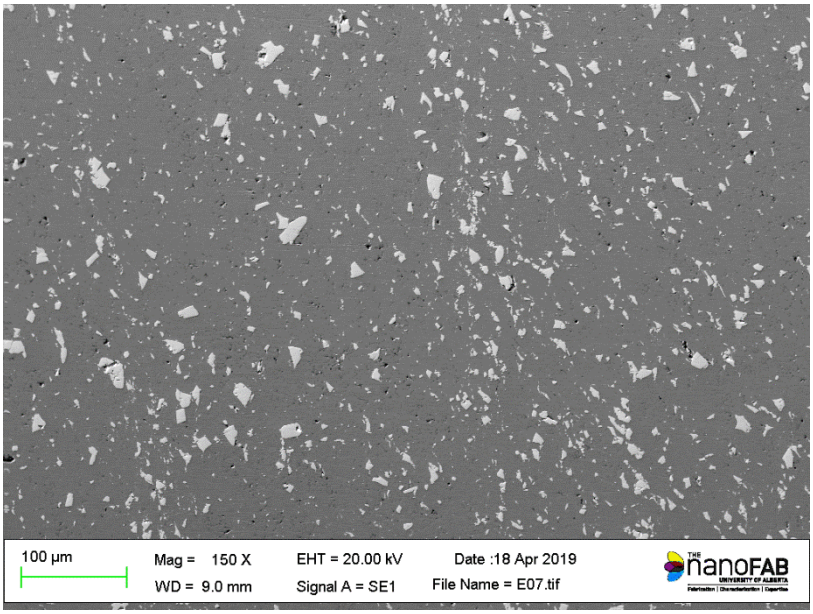

Figure B2: SEM image of the coating fabricated from the 71 wt.% WC + 29 wt.% Ni in the feedstock powder.

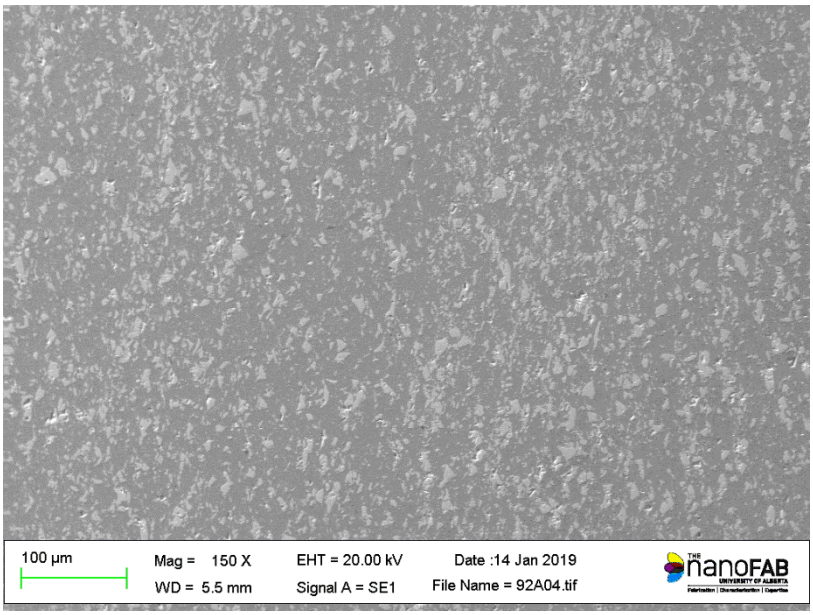

Figure B3: SEM image of the coating fabricated from the 92 wt.% WC + 8 wt.% Ni in the feedstock powder.